THE ASTROPHYSICAL JOURNAL, 466:254–273, 1996 July 20

ADAPTIVE OPTICS NEAR-INFRARED IMAGING OF R136 IN 30 DORADUS: THE STELLAR POPULATION OF A NEARBY STARBURST

B. BRANDL, B. J. SAMS, F. BERTOLDI, A. ECKART, R. GENZEL, S. DRAPATZ, R. HOFMANN, M. LÖWE,[1] AND A. QUIRRENBACH
Max-Planck-Institut für Extraterrestrische Physik, Giessenbachstrasse, 85740 Garching, Germany
Received 1995 August 23; accepted 1996 January 11

ABSTRACT

We report 0.″15 resolution near-infrared (NIR) imaging of R136, the central region of 30 Doradus in the large Magellanic Cloud. Our 12.″8 × 12.″8 images were recorded with the MPE camera SHARP II at the 3.6 m ESO telescope, using the adaptive optics system COME ON+. The high spatial resolution and sensitivity (20th magnitude in *K*) of our observations allow our *H*- and *K*-band images to be compared and combined with recent *Hubble Space Telescope* (*HST*) WFPC2 data of R136. We fit theoretical models with variable foreground extinction to the observed magnitudes of ∼1000 stars (roughly half of which were detected in *HST* and NIR bands) and derive the stellar population in this starburst region. We find no red giants or supergiants; however, we detect ∼110 extremely red sources which are probably young, pre–main-sequence low- or intermediate-mass stars. We obtained narrow-band images to identify known and new Wolf-Rayet stars by their He II (2.189 μm) and Brγ (2.166 μm) emission lines. The presence of W-R stars and absence of red supergiants narrow the cluster age to 3–5 Myr, while the derived ratio of W-R to O stars of 0.05 in the central region favors an age of ∼3.5 Myr, with a relatively short starburst duration. For the O stars, the core radius is found to be 0.1 pc and appears to decrease with increasing stellar mass. The slope of the mass function function is $\Gamma = -1.6$ on average, but it steepens with increasing distance from the cluster center from $\Gamma = -1.3$ in the inner 0.4 pc to $\Gamma = -2.2$ outside 0.8 pc for stars more massive than 12 $M_\odot$. The radial variation of the mass function reveals strong mass segregation that is probably due to the cluster's dynamical evolution.

Subject headings: H II regions — infrared: stars — ISM: individual (30 Doradus) — Magellanic Clouds — stars: early-type — techniques: image processing

1. INTRODUCTION

The 30 Doradus region in the LMC is the largest and most massive H II region in the Local Group. Within a diameter of 15′ (200 pc), it contains more than 8×10^5 $M_\odot$ of ionized gas (Kennicutt 1984), and the gas shows a highly fragmented shell-like structure in the Brγ line map (Poglitsch et al. 1995). Fast expanding shells with 100–5000 $M_\odot$ and kinetic energies up to 10^{51} ergs indicate several past supernova events (Kennicutt & Chu 1994). About 2400 OB stars in the inner 60 pc, known as the stellar cluster NGC 2070, produce approximately 4.5×10^{51} Lyman-continuum photons per second, which is 1/3 of the total ionizing radiation in the entire 30 Doradus region (Parker 1993; Walborn 1991). The bolometric luminosity of the inner 4.5 pc core of this cluster is 7.8×10^7 $L_\odot$ (Malumuth & Heap 1994) and hence much larger than in the Galactic H II regions such as Orion, W49, or NGC 3603. The stellar ages range from about zero (for the obscured protostellar regions) to 10–12 Myr (Melnick 1992, p. 253). The center of this stellar association, R136 (HD 38268), is an unusually high concentration of massive and bright O, B, and Wolf-Rayet stars. Standard ground-based observations suffering from atmospheric seeing show three main components in R136: a, b, and c. Of these, R136a was at one time thought to be the most massive star ever known, with a mass of about 2500 $M_\odot$ (Cassinelli, Mathis, & Savage 1981). Using speckle techniques, Weigelt & Baier (1985) demonstrated that R136a consists of at least eight stellar components. Subsequently, the *Hubble Space Telescope* (*HST*) observed R136a with its Faint Object Camera (FOC) (Weigelt et al. 1991; de Marchi et al. 1993), the Wide Field Planetary Camera (WFPC) (Campbell et al. 1992; Elson et al. 1992; Malumuth & Heap 1994; Parker, Heap, & Malumuth 1995; Hunter et al. 1995), the Fine Guidance Sensor (FGS) (Lattanzi et al. 1994), and the Goddard High-Resolution Spectrograph (GHRS) (Walborn et al. 1992; Heap et al. 1994).

Its large mass of ionized gas, a population with stellar masses over 100 $M_\odot$, and its relative proximity make R136 and its surroundings the closest example of a starburst region. Hence, it provides a unique laboratory for studying the fundamental physics of starbursts: How old is the central burst? Are stars still forming? Are there red giants? Are there low-mass pre–main-sequence objects or is there a rather high lower mass cutoff? How important is spatially variable extinction toward the individual stars for the population analysis? Does the mass function in the inner region differ from its surroundings, and, if so, is this a result of dynamical relaxation? Previous studies suffered from low spatial or spectral resolution; therefore, our observations investigate the properties of this starburst region via high-resolution photometry and line imaging. We report on near–diffraction-limited adaptive optics observations of R136 in the *H* and *K* bands and in the He II (2.189 μm) and Brγ (2.166 μm) lines. We combine our adaptive optics observations with recent WFPC2 measurements in the *U*,

[1] MPG Gruppe "Staub in Sternentstehungsgebieten," Schillergäßchen 2, 07745 Jena, Germany.

V and I bands (Hunter et al. 1995) to obtain multicolor photometric information from 0.3 to 2.5 μm. We then fit theoretical stellar models to the measured $UBIHK$ colors, accounting for spatially variable extinction, to derive the stellar population and dynamics of R136.

2. DATA REDUCTION

2.1. *Observations*

We used ESO's adaptive optics system COME ON+ (ADONIS) at the ESO 3.6 m telescope at LaSilla, Chile, together with the MPE near-infrared camera SHARP II. This joint system has produced many interesting observational results during its first 2 years in operation (Léna 1994). COME ON+ (Beuzit et al. 1995) was the first adaptive optics system open to the astronomical community. In 1995 January, it was mated to the user-friendly system ADONIS (Hubin et al. 1993). The shape of the atmospherically distorted wave front is measured at visible wavelengths, using a Shack-Hartmann wave front sensor. The correction for atmospheric turbulence is performed via a 52 piezo actuator deformable mirror that is driven by a closed online control loop with a correction bandwidth of up to 17 Hz. A reference source within the isoplanatic patch of the observed near-infrared (NIR) wavelength is needed for the correction. This source must be brighter than approximately 13th magnitude in V band and must possess either a bright, pointlike feature or an extended but unstructured brightness profile in order to be tracked properly by the wave front sensor. Due to its high spatial concentration, the central cluster of stars forming R136a can itself serve as the wave front reference.

The MPE SHARP II near-infrared camera (Brandl 1995b) is equipped with a 256×256 pixel Rockwell NICMOS III array detector and is optimized for high-resolution broad- and narrow-band imaging from 1.1 to 2.5 μm. The Nyquist sampling theorem requires at least two pixels across the FWHM (full width at half-maximum) of the point-spread function (PSF) in order to sample the beam sufficiently. SHARP II's image scale of 0".05 per pixel, resulting in a total field of view of 12".8 × 12".8, therefore provides the possibility of diffraction-limited imaging at wavelengths longer than 1.4 μm on the ESO 3.6 m telescope. Wide-band filters provide color discrimination in the J (1.10–1.40 μm), H (1.45–1.85 μm), and K (1.95–2.45 μm) bands, and a circular variable filter (CVF) covers the H and K bands with a spectral resolution $\lambda/\Delta\lambda \approx 60$. The total throughput of the camera optical system, including the quantum efficiency of the detector, is approximately 54% in the H band and 33% in the K band. The array detector is read out with four custom designed DSP boards (Hofmann et al. 1995), permitting integration times per frame ranging from several minutes down to 50 μs. For very short integration times a custom-made, cold mechanical shutter can be used. By the time this article is printed, a new version of the SHARP II camera will be available at ESO, offering different pixel scales and several spectroscopic utilities.

The present analysis is based on a total integration time of 190 minutes in K and 40 minutes in H, with an integration time per frame of 20 and 30 s, respectively. In order to identify Wolf-Rayet stars, we used the SHARP II CVF for observations in the He II$(10 \rightarrow 7)$ line at 2.189 μm, at 2.153 μm, covering the Brγ line, and at 2.240 μm for continuum subtraction. The total integration time was 32 minutes for the He II map and 20 minutes each for Brγ and spectrally nearby continuum measurements; the integration time per frame was 240 s.

Our observations of R136 were made on 1994 December 27 (K-band and emission lines) and 1995 March 10 (H band); the atomspheric conditions were fairly good with long-term optical seeing values below 1". We selected a field southeast of R136 with R136a near one array corner in order to cover a wide cluster radius and simultaneously get Melnick 34 (Mk 34), a relatively isolated, bright Wolf-Rayet (W-R) star which could be used as a PSF reference.

2.2. *Data Processing and Image Quality*

We corrected the image for bad pixels of the detector array (only 1%; no clustering or bad lines and columns). The sky frames used for subtraction from the on-source frames were calculated from the median of several field positions taken $\sim$1' away from R136. The flat field was produced from the average of several twilight sky frames which have more flux than a typical sky frame and hence reveal even very small variations in detector sensitivity.

The Strehl ratio (SR) is a useful measure for describing the quality of near–diffraction-limited imaging; it is defined as the peak intensity of the PSF normalized to the peak of a diffraction-limited Airy disk so that SR $\leq$ 1.0. A system is considered to be diffraction limited if SR $>$ 0.8. In a real astronomical optical system, the SR is reduced by wave front errors, originating either from static aberrations in the optical system itself or from insufficiently corrected atmospheric disturbances. The SR of sources in adaptive optics observations depends largely on the brightness of the wave front referencing object, its angular distance to the target object, and the actual seeing conditions. A typical adaptive optics PSF is characterized by a near–diffraction-limited spike on top of an extended ($\simeq$3".5), Gaussian-like seeing "background," plus some artificial structure due to insufficiently corrected low-order aberrations. In order to calculate a "practical" Strehl ratio, we computed the two-dimensional Airy function on a 256×256 pixel grid, corresponding to diffraction-limied imaging. This Airy pattern was shifted to the actual source peak position (on a finer subgrid) and normalized to the measured source flux. Our SR is the ratio between the brightest pixel in the measured PSF and the theoretical diffraction pattern, taking the central obscuration of the telescope secondary mirror into account. For this calculation, we took only relatively bright and isolated sources at different distances from the wave front reference (in this case the cluster center). If the extended background contains a significant amount of flux due to uncorrected higher order modes, this leads to a relatively small SR. The almost diffraction-limited spike, however, is not affected by the surrounding halo, and the spatial resolutionin the image is indeed better than the Strehl value indicates.

We achieved a SR of 24% for the H-band observations, which is in good agreement with the system specifications for comparable observing conditions (ESO 1995); the width of the "raw" PSF is FWHM (H band) $\approx$ 0".18. The SR of about 17% for the K-band data is slightly worse than expected, for reasons discussed below. The H-band data show a spatially constant value of the SR within $\approx$12".5 (see Fig. 1), emphasizing the excellent atmospheric conditions during that night. Therefore, assuming a constant PSF for all stars in the H-band image seems to be reasonable. The

K-band data, taken in December under similarly good atmospheric conditions, show a significant amount of additional triangular coma-like aberrations, inherent in all sources, but with varying strength. Each PSF has two "coma wings" separated by $\approx 0\farcs23$ to the southeast and the north, with relative peak intensities of roughly 1/3 and 1/10 of the central peak, plus a slight elongation to the southwest. This aberration is independent of the actual atmospheric conditions and was probably introduced somewhere in the adaptive optics optical system itself. Figure 1 shows the relative amount of "coma intensity." The central source peak is still quite compact [FWHM (K band) $\approx 0\farcs19$, compared to $0\farcs15$ for diffraction-limited imaging], but the SR is smaller than in the H-band data, due to missing flux contained in the "coma peaks."

We applied the Lucy-Richardson deconvolution algorithm (Lucy 1974) to "CLEAN" the image of the effect of the "dirty" beam. We did not attempt to obtain superresolution. The algorithm, as it is implemented in our IRSI software package (Eckart & Duhoux 1990), is an iterative nonlinear deconvolution method based on the comparison of the untreated input map with the current estimate of the deconvolved map, reconvolved with the PSF. We took the W-R star Mk 34 to derive the PSF reference after removing iteratively several faint neighboring sources. For the K-band image, we calculated a mean PSF from different stars, accounting for the spatial variations described above. After a sufficient number of iterations, the deconvolution program converges to the maximum likelihood solution. We used 4000 iterations for R136, resulting in a map of delta functions which were then reconvolved with a Gaussian restoring beam that corresponds to the diffraction limit of the 3.6 m telescope: $0\farcs15$ in K and $0\farcs12$ in the H band.

Figure 2 shows a contour plot of the resulting H-band image. For the first time at NIR wavelengths, the crowded core of R136a is resolved into its individual components. Our map shows excellent agreement with recent *HST* images as far as the spatial resolution and the source positions are concerned. We also present a log-scaled K-band image in Figure 3 (Plate 13); color images showing a comparison with *HST* data have already been presented by Brandl et al. (1995) and Brandl (1995). The faintest ($>3\ \sigma$) sources are 20th magnitude in K; thus, the dynamical range in the image is roughly 9 mag. However, toward the crowded central region, faint stars in the vicinity of brighter stars remain undetected. Previously cataloged stars within our field of view are listed in Table 1.

2.3. *Photometric Analysis*

2.3.1. *The Photometry Package PLUCY*

Determining photometric fluxes in crowded star fields is a complex issue and requires careful testing and comparison of different methods. The special properties of R136 require a photometric program which satisfies at least these three requirements: (i) the derived source fluxes should be insensitive to inaccuracies in a constant background subtraction; (ii) spatial variations in the background (e.g., nebular emission within the cluster) should be taken into account; (iii) it should be possible to analyze over 1000 stars simultaneously. We investigated several techniques, including circular aperture photometry with different sized apertures on the raw δ-function maps (produced by the Lucy-Richardson algorithm) and the DAOPHOT package (Stetson 1987). Ultimately we chose the PLUCY photometry package (Lucy 1994; Hook et al. 1994), a two-channel photometric image restoration program which fulfills all the requirements listed above. Since use of PLUCY is not yet very widespread, we give a short description of the basic principle:

The true intensity distribution on the sky at the jth pixel, Ψ_j, is considered to be the sum of a smooth extended light distribution ψ_j (e.g., background from the instrument or sky plus extended nebular emission) and the source fluxes ψ_j^*. The latter image is zero everywhere except for δ-functions at the positions of designated point sources. Starting from an initial guess (which may be $\sum \psi_j = \sum \psi_j^* = \frac{1}{2}$), the algorithm iteratively maximizes an objective function Q which is the sum of a likelihood and an entropy term:

$$Q = \sum_j I_j \ln(\Phi_j) - \underbrace{\alpha \sum_j \psi_j \ln \frac{\psi_j}{\chi_j}}_{\text{background}}, \qquad (2.1)$$

where I_j is the observed intensity distribution, Φ_j is the estimate of that distribution, and α controls the strength of regularization ($\alpha = 0$ corresponds to the standard Lucy-Richardson algorithm). The term χ_j is a "floating default" image, and in this implementation it is obtained by smoothing the current estimate for the background (ψ_j) with a Gaussian kernel. Convergence is usually reached after several tens of iterations.

The source positions in PLUCY must be known in advance. Therefore, we compared the local maxima positions in our deconvolved NIR maps to the WFPC2 maps (Hunter et al. 1995). Since the alignment uncertainty is less than $\pm 0\farcs075$, we generated a common source position list which served as the input list for PLUCY.

We took measurements of two nearby standard stars (Bouchet, Manfroid, & Schmider 1991) plus one standard star at approximately the same air mass, for flux calibration: HD 38921 (SAO 196100) of spectral type A0 V, HR 2015 (δ Dor) of spectral type A7 V, and BD $+0\fdg1694$ (HD 292693) of spectral type K7 V. The flux differences were less than 0.01 mag in K. The H-band measurements taken on two nights, one of which had cirrus clouds, varied by 0.28 mag; hence, we calibrated the flux based on the unclouded night for the H band, and on all nights for the K band. Furthermore, we made some additional fine correction to the photometry as described below. We took the distance modulus to the LMC to be -18.57 mag.

2.3.2. *The Photometric Errors*

Proper evaluation of photometric errors is fundamental to our analysis. In general, there are two potential contributions that account for photometric errors in crowded fields: (1) the flux determination for known sources separated by less than the FWHM of the PSF is uncertain ("crowding"); (2) undetected faint stars may enhance the intrinsic flux of brighter sources ("blending"). We estimated the photometric errors by producing an artificial "delta map" with values according to the H-band flux and location of the sources. The peaks were shifted randomly by ± 1 pixel to account for source position uncertainties, and the result was reconvolved with the H-band PSF. Appropriate noise, taken from our sky frames, was added. The flux information from PLUCY was compared to the input fluxes; the photo-

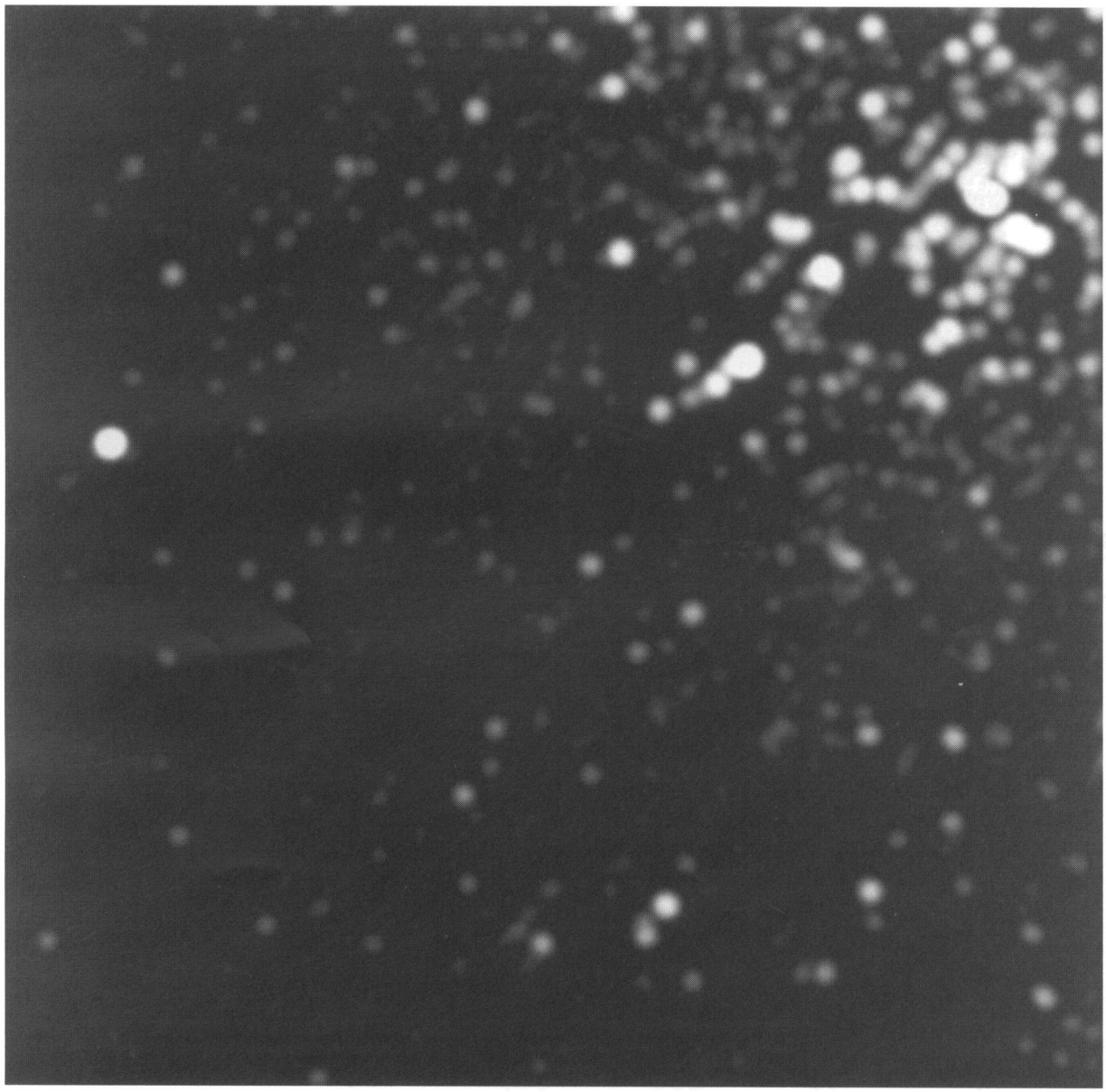

FIG. 3.—190 minute *K*-band exposure of R136. The field of view is 12.″8 × 12.″8, corresponding to 3.2 × 3.2 pc^2. North is up, and east is to the left. The spatial resolution after deconvolution is 0.″15 FWHM; logarithmic scaling has been used. The faintest stars visible have 20th magnitude in *K*.

BRANDL et al. (see 466, 256)

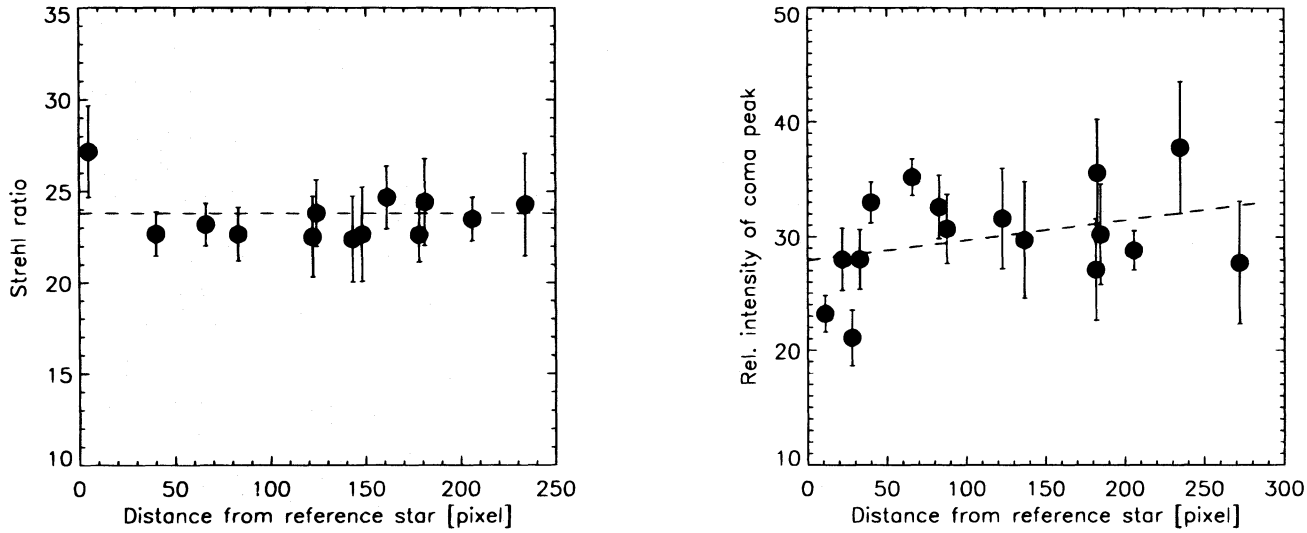

FIG. 1.—*Left*: The Strehl ratio (in %) in our *H*-band data for several sources at different distances from the wave front reference in pixels. The constant value excludes spatial variation of the PSF as a relevant source of photometric errors. *Right*: The intensity ratio of the "coma peak" to the main source peak in the *K*-band data (in %). The values are between 20% and 40%, increasing slightly with the distance to the center.

metric accuracy is shown in Figure 4. There is very little scatter of the bright sources; for faint sources, the results are somewhat worse than those described by Hook et al. (1994).

Another possible source of error that has to be considered, particularly in adaptive optics observations, is a spatially varying PSF. This is particularly important for observations in which the wave front reference source is outside the field of view or spatially separated by more than the isoplanatic patch size from the target. Since the reference source lies within our relatively small field of view and the seeing conditions were excellent, spatial variations of the PSF are not important for our observations, as we have already shown in Figure 1. However, the photometric uncertainties in the *K*-band map can be severe for faint sources that are affected by the "coma wings" of a bright neighboring source. Fortunately, these cases show an obviously enhanced *K*-band magnitude relative to their *UVIH* magnitudes. We checked the positions of the affected sources relative to their neighbors. In cases of blending by the coma-like structure (only 26 sources), their *K*-band magnitudes were ignored in the further analysis.

3. IDENTIFYING STELLAR TYPES

Now we derive the stellar population in R136 by comparing the measured stellar luminosities to theoretical model calculations for each individual star. In order to cover the widest possible wavelength range, we combine the data from our high spatial resolution *H*- and *K*-band maps (0.″15) with recent WFPC2 observations (~0.″06 resolution in *V*), which were taken in the F336W, F555W, and F814W

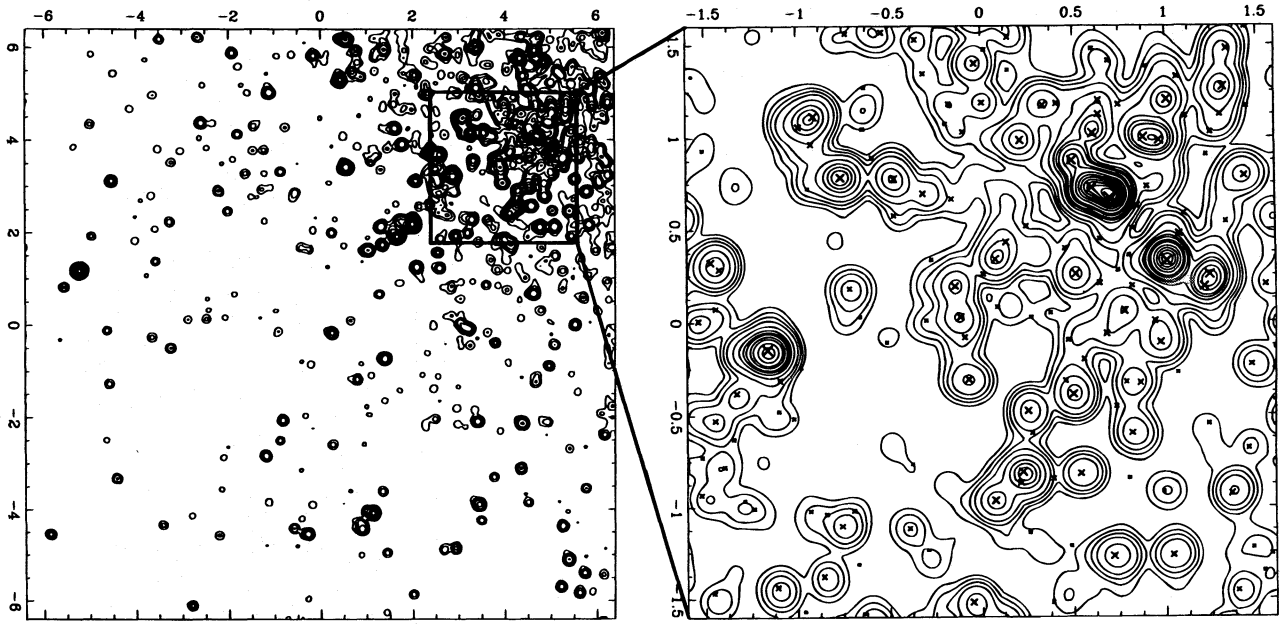

FIG. 2.—Contour plot of our 12.″8 × 12.″8 field of view in *H* band. The contour levels are at 0.1, 0.25, 0.5, 1, 2.5, 5, 10, 25, 50, 75, and 100% of the maximum intensity, which corresponds to 11.2 mag in *H* band. North is up, and east is to the left. The spatial resolution is 0.″12. The inset enlarges the central 3.″2 × 3.″2. Crosses indicate the positions of the sources detected by *HST*; their size is according to the measured *V* magnitudes.

TABLE 1

POSITIONS OF PREVIOUSLY CATALOGED STARS WITHIN OUR FIELD OF VIEW

H Number	M Number	Name	Spectral Type	x	y	α(2000)	δ(2000)	U	V	I	H	K
3	498	R136a1	WN	411	57	42.43	02.″2	−8.77[a]	−7.34[a]	−7.29[a]	−7.59[a]	−7.68[a]
17	...	R136a1B	...	413	56	42.43	02.2	...	...	...	...	...
5	511	R136a2	WN4-w	413	61	42.45	02.2	−8.13	−6.84	−6.79	−6.92	−6.93
6	467	R136a3	WN	397	45	42.37	02.6	−8.21	−6.79	−6.81	−7.11	−7.09
21	474	R136a4	...	423	47	42.38	01.9	−7.95[a]	−6.47[a]	−6.28[a]	−6.15[a]	−5.65[a]
20	519	R136a5	Of3/WN	419	66	42.47	02.0	−7.30	−5.87	−5.73	−5.67	−5.32
19	454	R136a6	...	394	36	42.33	02.7	−7.95[a]	−6.51[a]	−6.34[a]	−6.34[a]	−6.42[a]
24	509	R136a7	...	425	61	42.45	01.9	−7.23	−5.74	−5.61	−5.26	−3.96
27	480	R136a8	...	424	50	42.40	01.9	...	...	...	...	...
9	637	R136b	Of/WN	378	132	42.78	03.1	−7.78	−6.48	−6.51	−6.73	−6.67
10	681	R136c	WN	337	168	42.95	04.2	−7.55	−6.33	−6.56	−7.32	−7.47
8	880	Mk 34	WN4.5	297	455	44.30	05.3	−7.83	−6.50	−6.50	−6.93	−7.02
41	716	Mk 35N	O5–7 V	87	204	43.09	10.9	−6.66	−5.18	−4.94	−4.66	−4.65

NOTES.—The star numbers are from Hunter et al. 1995 (H) and Malumuth & Heap 1994 (M). Stellar types are based on measurements by Melnick 1985, Campbell et al. 1992, Parker et al. 1995, and Heap et al. 1994. x and y are pixel coordinates on our 256 × 256 detector, expressed as 512 × 512 for a more accurate source location; (0, 0) corresponds to the lower right corner in the contourmap. The pixel row orientation on the detector is parallel to the N-S/E-W direction to within 3°. Zero coordinates are R.A.(2000) = 05^h38^m, decl.(2000) = −69°06′. Our field of view covers the area α(2000) = $05^h38^m42.^s17$–$44.^s52$; δ(2000) = −69°05′59.″7–06′12.″5.

[a] Due to crowding, three star pairs, H(3 + 17), H(19 + 26), and H(21 + 27), could not be photometrically resolved (star 26 has no specific name and is therefore not listed here). We added the fluxes and give the combined magnitude only for the first member of each pair.

filter bands (Hunter et al. 1995). The combined *HST* and SHARP II data provide good photometric information on more than 1000 individual stars, roughly half of them in four or five bands (*UVIHK*). The wide spectral coverage (0.33–2.45 μm) enables us to match accurately the observed stellar fluxes with stellar photometric models. We computed these models by combining recent stellar evolution calculations (Schaerer et al. 1993) with the Kurucz (1992) Atlas 9.3 model atmosphere grid. This approach enables us to derive an estimate for the star's age, initial mass, and foreground extinction. With additional information from our He II and Brγ line maps, we are further able to identify Wolf-Rayet stars, most of which were known from previous observations.

3.1. *Combining Adaptive Optics and HST Data*

The combined WFPC2 source list contains 1090 sources within our field of view, of which we detected 531 in either H or K band; 498 of these were detected in both H and K bands. Three hundred forty-one sources have reliable flux information in all five bands, and more than 657 sources were detected in at least three bands. With only five exceptions, all stars brighter than $V = 16$ mag were detected in the NIR. Most of those we did not detect are either very faint blue sources with $V > 20$ mag or were detected in only one of the *HST* bands.

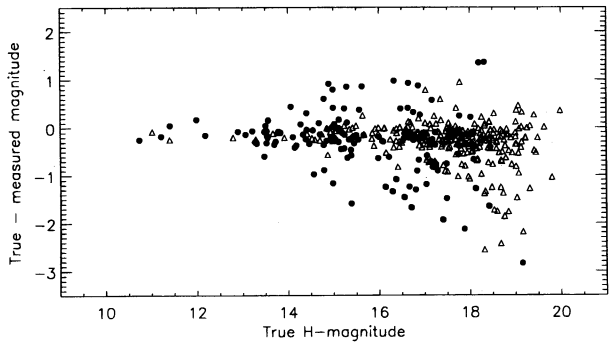

FIG. 4.—The photometric accuracy of the PLUCY program in the crowded R136 region (see text). Shown is the difference between true and measured magnitude, depending on the true magnitude of the source. Sources with values below zero appear to be bluer due to missing IR flux for given UVI magnitudes. Filled dots indicate sources inside the central 3.″3 around R136a1; triangles indicate sources outside the central region.

In addition, we find 58 red sources not detected in *UVI*; 26 of them have reliable flux information in both H and K bands and were included in our final analysis. The large overlap in the SHARP II and *HST* source lists illustrates the comparable sensitivity limit of both observations.

We converted the *HST* F336W, F555W, and F814W filter band magnitudes into ground-based U- and V-band magnitudes through the relations U = F336W + 0.30 and V = F555W − 0.06 (Hunter et al. 1995). The F814W filter, here referred to as the I band, is centered at 0.814 μm with a spectral width of 175.8 nm; we applied no ground correction to this band. As indicated in Figure 4, there may be a small calibration offset to our photometric data. We found that adding 0.05 mag to our H and K magnitudes yielded an overall better fit between the data and the models; thus, $H' = H + 0.05$ and $K' = K + 0.05$ are the magnitudes used to compare with the models.

3.2. *Photometric Models*

Schaerer et al. (1993) computed a grid of stellar evolution models at initial metallicity, $Z = 0.008$, close to that observed in the LMC (Kontizas, Kontizas, & Michalitsianos 1993). On an initial mass grid (2, 3, 4, 5, 7, 10, 12, 15, 20, 25, 40, 60, 85, 120) $M_\odot$, they derive the star's present mass, bolometric luminosity, and effective surface temperature as a function of time. Meynet et al. (1994) complemented these models with a set of tracks assuming a mass loss enhanced by a factor of 2 for $12\ M_\odot < m_0 < 120\ M_\odot$. Since the mass loss of the massive stars in R136 is observed to be significantly higher than for comparable galactic stars (Heap et al. 1994), we used the Meynet et al. models for $m \geq 12\ M_\odot$. Low-mass stars ($m < 5\ M_\odot$) can spend a significant time (i.e., comparable to or longer than the estimated age of R136) in a pre–main-sequence (PMS) phase, in which the star's luminosity is governed by gravitational contraction and deuterium burning. Schaerer's models do not account for PMS evolution. Since main-

sequence stars less massive than 10 $M_\odot$ evolve little in their initial 10 Myr, we have interpolated the L_{bol} and T_{eff} of Schaerer's models to add additional mass points at 6, 8, and 9 $M_\odot$. For each mass point, we also interpolated the time grid into smaller time steps between the points given by Schaerer et al.'s evolution models. In addition, young low-mass stars may show a significant IR excess due to a circumstellar disk. Because of such theoretical uncertainties in existing PMS stellar evolution models, and since our images do not reach deep enough to detect many low-mass stars, we have not attempted to account for the PMS evolution of the low-mass stars. All quoted ages should therefore be understood as the time from the zero-age main sequence (ZAMS).

3.3. *Model Atmospheres*

We combined the Kurucz (1992) ATLAS 9.3 stellar atmosphere models with the Schaerer et al. stellar evolution models to determine the photometric band magnitudes of a star of given mass as a function of time. We did not derive model spectra for the W-R phase, since W-R star emission is governed by the complex line and continuum radiation transfer in an optically thick wind which is unaccounted for in the Kurucz models. Kurucz's models cover temperatures up to 50,000 K, so that for the most massive stars we needed to extrapolate toward higher temperatures by assuming blackbody emission, or adopting non-LTE models (Kunze, Kudritzky, & Puls 1992), which are in good agreement with those of Kurucz at $T_{eff} > 25{,}000$ K. The bolometric magnitudes were computed from the effective temperature T_{eff} and the radius r as $M_{bol} = -10 \log (T_{eff}[r/r_\odot]^{1/2}/17{,}200\ K)$. The band magnitudes were derived using the Johnson system (Johnson & Morgan 1953) and were calibrated with the following zero magnitude fluxes in units of [ergs cm^{-2} s^{-1} nm^{-1}]: U, 4.27×10^{-8}; V, 3.64×10^{-8}; I, 1.12×10^{-8}; H, 1.19×10^{-9}; and K, 4.17×10^{-10}. From the combined stellar evolution and atmosphere models, we thus derive $UVIHK$ band luminosities on a two-dimensional grid of stellar mass and age. Figure 5 shows the U- and K-band luminosity evolution for stars of different masses.

3.4. *Extinction and Reddening*

From detailed studies of dense galactic H II regions, we know that the extinction can vary significantly on subparsec scales due to, e.g., windblown bubbles and shells, or dense flows from photoevaporating gas clumps and circumstellar disks (Bertoldi & Jenkins 1992); hence, we allow for variable extinction (and thereby reddening) for each source. In addition to this spatially variable local extinction, there is an average reddening toward R136 that consists of three components: absorption in our Galaxy with $E(B-V) = 0.07$, LMC foreground reddening with $E(B-V) = 0.16$ (Fitzpatrick 1985), and absorption within the 30 Doradus/R136 region. Previous analyses assumed a constant reddening value, which varied from $E(B-V) = 0.53$ (Campbell et al. 1992) to 0.38 (Hunter et al. 1995). We left the extinction a free parameter that is to be determined for each star individually. We assumed the "universal" reddening law (Rieke & Lebofsky 1985), so that the extinction magnitudes relate as $A_x/A_v = (1.531, 1.324, 0.6, 0.175, 0.112)$ for $x = (U, B, I, H, K)$. We fitted the models to the measured band spectra by minimizing the residuals on a three-dimensional grid of ZAMS stellar mass m_0, age t, and extinction A_V. A typical case is presented in Figure 6 for the spectroscopically known O5–7 main-sequence star Mk 35N (our star number 41).

3.5. *Fit Accuracy*

To test our fitting algorithm, we fitted UBV band model tracks to 30 Doradus OB stars (Schild & Testor 1992) with spectroscopically determined spectral types. For most stars, our identifications were in agreement with the spectroscopically derived types within one spectral subclass. Taking near-infrared colors into account, the fit accuracy could be improved significantly. We tested our fit routine (with solar metallicity) on several galactic infrared standard stars and also found good agreement. However, there are some exceptions to this, which we detail below.

Since the luminosity evolution within the first 10 Myr of stars less massive than about 10 $M_\odot$ is less than about 0.5 mag and is thereby comprable to the luminosity difference between adjacent mass points, the age estimates we derive for stars with $M \lesssim 10\ M_\odot$ are somewhat uncertain. For

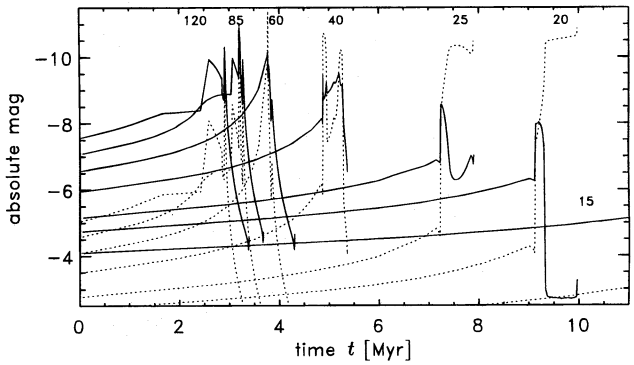

FIG. 5.—The U (*solid line*) and K (*dotted line*) luminosity evolution of stars with different ZAMS masses as a function of age. Stars with $m \leq 25\ M_\odot$ become red supergiants, whereas more massive stars turn into red supergiants, high-mass-loss WN stars, and finally into increasingly hotter WC stars. Supergiants are identified easily from their $U-K$ color, demonstrating the need to cover a large wavelength range to identify stellar types.

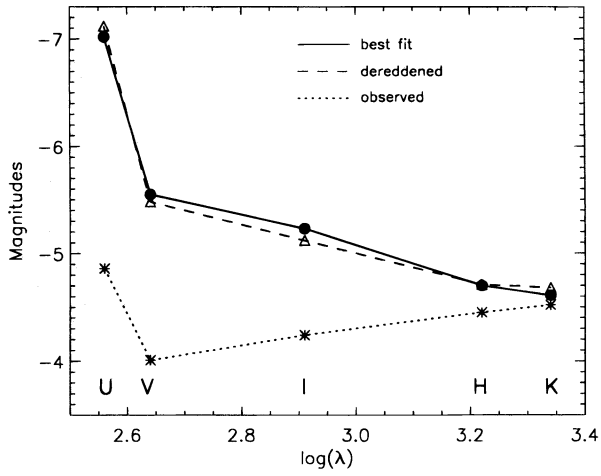

FIG. 6.—Fitting the spectroscopic O5–7 main-sequence star Mk 35N (our number 41). The observed $UVIHK$ magnitudes (*asterisks connected by dotted line*) were derived by subtracting a distance modulus $D_l = 18.57$. The closest match between the observed band spectrum and a model spectrum required a dereddening by $A_V = 1.47$ (*solid line*) to match the spectrum of a 1.5 Myr old 60 $M_\odot$ star (*triangles and dashed line*), consistent with the spectroscopic classification.

example, an 8 $M_\odot$ star at 10 Myr has a similar luminosity as a 9 $M_\odot$ star at ZAMS, the 8 $M_\odot$ star being only slightly redder. Given our photometric uncertainties, it is thus difficult to distinguish between, for example, the two alternative identifications, 8 $M_\odot$/10 Myr, and 9 $M_\odot$/0 Myr. Hence, the estimated age of stars $\leq 12\ M_\odot$ are not reliable.

In the derived age distribution (Fig. 13), we found a significant overabundance of stars with ages equal to the first time step at given mass. The error between the observed color and the model identification for these stars is also higher than for other age identifications. This overabundance is due to the coarseness of our mass grid. A star that our algorithm identified, as, e.g., 12 $M_\odot$ at age 0.1 Myr may be better fit by an 11 $M_\odot$ star at several Myr age, for which we have no color information. Thus, most identifications of stellar ages between 0 and 0.1 Myr should be considered unreliable.

About two dozen low-mass stars were best fitted with ages of several hundred million years. Those low-mass stars show only little luminosity evolution on the main sequence, and the observed fluxes would also be in good agreement with stars of a few million years. Since this affects only the identification of a few low-mass stars, and their high fitted ages are due to small photometric uncertainties rather than significant luminosity evolution, we restricted the ages allowed in the fit to a maximum of 7 Myr.

Deriving the ZAMS mass of massive stars via photometry using broadband colors alone is difficult (Massey et al. 1995, and references therein). For example, there is only a difference of about 0.03 mag in $(B-V)_0$ between a B0 V and an O3 V star, and even the change in $(U-B)_0$ between an O9 V and an O3 V star is less than 0.10 mag. These values lie typically within the uncertainty of the color calibration. Adding two NIR photometry bands to the three visual improves the identification in two ways. The color differences are larger, e.g., $(U-K)_0$ between a 60 $M_\odot$ and a 15 $M_\odot$ main-sequence star ranges between 0.10–0.19 mag, depending on age. Furthermore, the photometric errors are reduced significantly by "averaging" over five measurements.

A coeval population of main-sequence O stars covers over 3 mag in luminosity. If all stars in R136 were at the same age, discriminating the stellar types would be easy, even if they had variable foreground extinction and reddening. However, luminosity evolution of the most massive stars within only a few million years produces luminosity variations comparable to the ZAMS luminosity difference between stellar types. For example, a 40 $M_\odot$ star at 4 Myr has $B = -6.10$ mag and is brighter than an 85 $M_\odot$ star ($B = -5.93$ mag) at ZAMS. The ambiguity due to a possible age spread can be only partially resolved by comparison of the star's colors. If independent evidence can narrow the age spread of the cluster (e.g., abundance of W-R stars, absence of red giants), the accuracy of the mass determinations is improved.

In order to estimate quantitatively the reliability of our mass determinations, and its dependence on the photometric noise level and the spread in reddening, we simulated "observed" photometric band magnitudes and tried to recover the stars' masses.

To the theoretical *UVIHK* magnitudes of 54 OB stars at different ages, we randomly added dust extinction with a distribution similar to that observed, plus typical measurement errors. The latter have a Gaussian distribution with half-maximum values of 0.3 mag in *H* and *K*, and 0.15 mag in *UVI* (see Fig. 3). Each of the 54 model stars was thereby multiplied 100 times, and the resulting set of 5400 stars was analyzed by our fit program under different age constraints. The result is shown on the left in Figure 7, where the abscissa indicates the "true" ZAMS mass, and the ordinate indicates the ZAMS mass which was assigned by the fit program. The size of the dots corresponds to the number of stars in each identification bin. The vertical scatter is a measure of the uncertainty of the mass identification; it is very small for stars less massive than 20 $M_\odot$ but becomes significant for the O stars. More than half the 60 $M_\odot$ stars in our sample were identified as 25 $M_\odot$ or 40 $M_\odot$ stars, and some were even identified as 85 $M_\odot$ or 120 $M_\odot$. Fortunately, however, this dispersion would not unduly affect our statistical analysis of the global cluster properties.

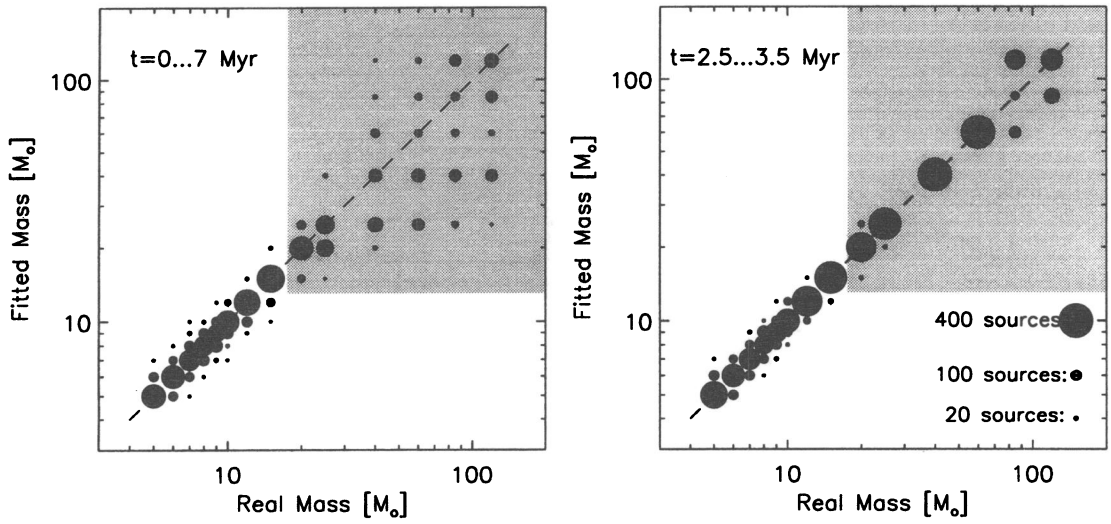

FIG. 7.—Fitted star ZAMS masses vs. actual masses from a sample of 5400 main-sequence stars of different stellar types and ages with random extinction and measurement errors (see text). The size of the dots corresponds to the number of stars identified at this mass. The gray shaded area indicates the mass regime of O stars.

In order to study the cluster's global properties, we do not need accurate individual star masses. Our O-star test sample contains a total mass of 115,600 $M_\odot$. the stars that were fitted with too small a mass have 42,375 $M_\odot$; those with too high a mass add to 31,995 $M_\odot$. A total of 41,230 $M_\odot$ were assigned correctly. The total fitted mass is only 17% lower than the original mass. Since our test sample has a flat mass spectrum and the probability of misidentification increases with mass, the total effect on a sample with a "standard" Salpeter (Salpeter 1955) or Miller-Scalo (Miller & Scalo 1979) initial mass function (IMF) would be less significant. From our statistical tests, we estimate a typical error of 30% in the fitted mass of an O star.

As we will show in § 4.3, we can restrict the cluster age by the relative abundance of stellar types. Since luminosity evolution is the main source of misidentifications, a restriction of the possible age will result in a more precise mass determination. This is demonstrated in Figure 7, where we show the results of a test on a set of stars with "true" ages between 2.5 and 3.5 Myr, and the same age constraint to the fit program. We see that the number and spread of misidentifications is much reduced over the previous test set: less than 1% of the initial total mass is missing in the fit masses, and misidentified stars are only shifted to their neighboring mass bin. Therefore, we will compare the results on mass function and core radius in § 4 with those derived by a fit restricted to 2.5–3.5 Myr. This yields another possibility to check the reliability of our approach.

4. RESULTS

We derived reliable photometric fluxes for most sources in our source list, except for some fainter sources for which our photometric accuracy test indicated uncertain photometric information. The fitting procedure processed a total of 634 sources with reliable fluxes in at least three bands, excluding the candidate W-R stars. Out of these sources, 82 could only be matched to model spectra with an extinction in excess of $A_V = 3$ mag, or with $A_V > 2$ mag but unusually large residuals between the observed and model fluxes. These sources were selected out as candidate young stellar objects (YSOs) with IR excess emission due to circumstellar disks or cocoons (see § 4.2.2). For the remaining 552 sources, we derive reliable mass estimates.

4.1. *Extinction*

Figure 8 shows the numerical and spatial distribution of extinction for 634 sources with reliable photometry in at least three bands. Most stars show extinctions in excess of the $A_V = 0.71$ mag expected to arise from foreground extinction from our Galaxy plus the LMC in the direction of 30 Dor. Our median extinction is close to the $A_V = 1.17$ mag, corresponding to $E(B-V) = 0.38$, assumed by Hunter et al. It appears that the stars in the core of the cluster show almost no extinction in excess of the Galaxy plus LMC foreground. One possible explanation for this could be a lack of dust or gas in the central region, due to, e.g., a wind or supernova blown bubble. Since the extinction hole coincides with the dense cluster of W-R stars, this is a reasonable interpretation. The stars surrounding the core, however, show correlated, enhanced extinction. Note that $A_V = 1$ mag excess extinction corresponds to a gas column density of 6×10^{21} cm^2, which on a scale of 1 pc corresponds to a gas density of 2000 cm^{-3}, a density not atypical inside young galactic H II regions (e.g., the Trapezium). The photoevaporation of YSO circumstellar disks by the massive stars in the core could well serve as a long-term source of gas in the inner region of a young H II region and can result in an inside-out density gradient (Bertoldi & Jenkins 1992).

An alternative explanation for the extinction hole in the cluster center could be a systematic photometric error due

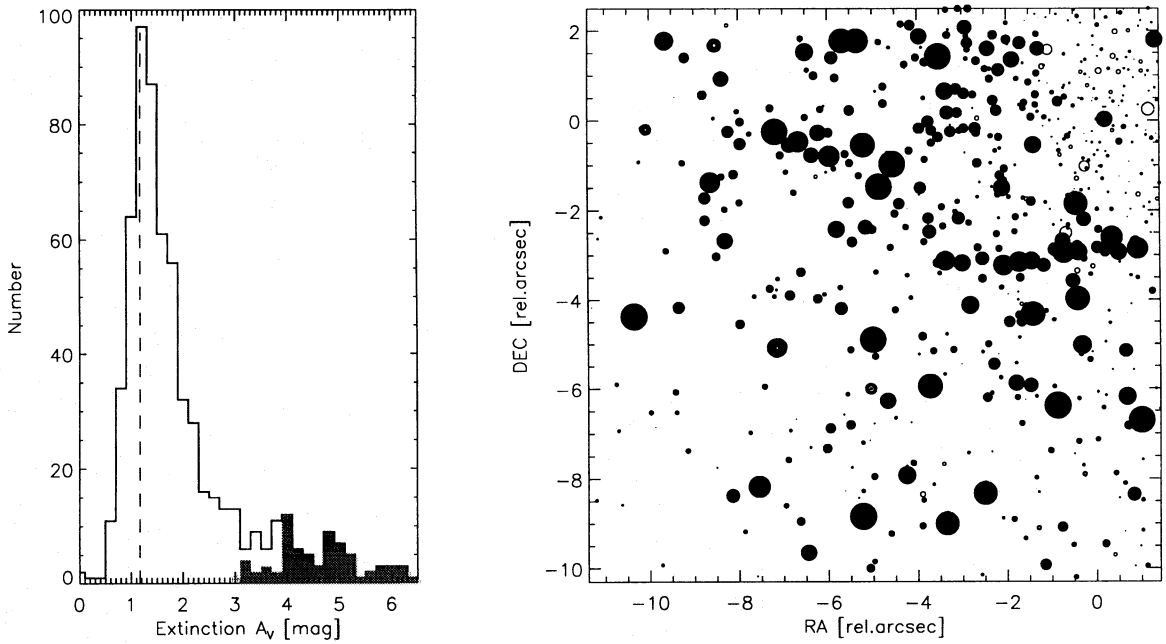

FIG. 8.—*Left*: Distribution of the individual stellar extinctions for the 634 sources which were detected in at least three bands. Milky Way plus LMC foreground extinction contribute $A_V = 0.71$ mag. The Hunter et al. mean value of $A_V = 1.17$ mag is indicated by the vertical dashed line. *Right*: Spatial distribution of the individual stellar extinction. The size of the dots indicates the amount of extinction in excess of the Milky Way and LMC foreground $A_V = 0.71$ mag. Open circles correspond to $A_V < 0.71$ mag; the largest dots correspond to $A_V = 3$ mag. The "red" sources corresponding to the shaded region in the left figure were excluded. Axis coordinates are in arcseconds relative to R136a1.

to crowding of the most luminous sources. If we had systematically underestimated the NIR luminosities of the sources in the cluster center, this would have led to apparently bluer colors and smaller reddening corrections. However, our photometric tests (Fig. 4) do not show a systematic flux decrease for sources with $H < 16$ in the inner cluster; the error dispersion far exceeds any systematic flux quenching, and since we do not find large reddening fluctuations, we favor a real extinction hole.

4.2. *Derived Stellar Population*

4.2.1. *The Wolf-Rayet Stars*

The continuum and strong line emission of Wolf-Rayet stars depends on complex non-LTE transfer effects in their winds; hence, there is presently no accurate NIR photometric model for such stars. Thus, we used the SHARP II CVF to identify Wolf-Rayet WN-type stars spectroscopically. We did not attempt to search specifically for WC-type stars, since all previous observations have only shown WN-type features within R136. Ten years ago, Melnick (1985) derived the stellar types of bright stars in the vicinity of R136, although his ground-based spectra did not resolve the individual central components. Previous measurements with the *HST*/PC6 in the narrow-band He II(468.6 nm) filter (Campbell et al. 1992; Parker et al. 1995), and GHRS spectroscopy of individual stars in the very center of R136 (Heap et al. 1994) have identified several W-R stars. Table 1 lists the main W-R components of R136 plus two spectroscopically known stars outside the central region but within our field.

WN stars are subdivided into the spectral types WN2–9 according to the strength of their emission lines: smaller numbers signify stars with stronger lines of more highly ionized atoms. The WN2–5 stars form the "early" WNE subgroup, whereas WN6–9 are "late" type WNL stars, although WNL stars are physically younger than WNE stars. The NIR provides important W-R line diagnostics, such as Brγ at 2.166 μm [which almost coincides with He II($14 \rightarrow 18$) at 2.165 μm], He I($10 \rightarrow 7$) at 2.058 μm, and He II($10 \rightarrow 7$) at 2.189 μm. Normal O stars show Brγ and He II in absorption, although He II emission has recently been observed in extreme Of stars (Conti et al. 1995). WNL stars show strong Brγ and He I, but weak He II emission. WNE stars have strong He II lines but weak Brγ emission. Approximate spectral classifications of WN stars can thus be based on their IR spectra (Crowther & Smith 1996); several typical spectra (from Eenens et al. 1995) illustrate this in Figure 9.

To identify WN stars, we took CVF measurements of He II and Brγ emission lines plus a continuum measurement at 2.240 μm. One continuum channel sufficed because the differences in the spectral indices of the brightest stars are small and the calibrations could be checked from spectroscopically known stars in our field. We cross-calibrated our line and continuum maps using the fluxes of about 20 OB stars and the O5–7 V star Mk 35N. The right contour plot in Figure 10 shows our He II line map of the central $4'' \times 4''$, continuum subtracted and normalized to the continuum flux of each source. The Brγ map was adjusted such that the flux from the precisely determined WN 4.5 star Mk 34 is equal in both He II and Brγ maps. Since this is an adjustment relative to the He II map, WN stars later than WN 4.5 should clearly appear in the Brγ map (Fig. 10, *left*).

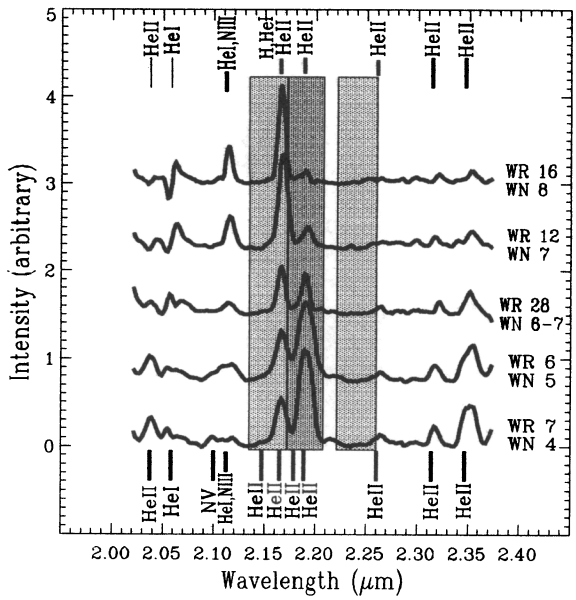

FIG. 9.—*K*-band spectra of different WN-type W-R stars, obtained at the Cerro Tololo Inter-American Observatory 4 m telescope (Eenens et al. 1995). The three spectral regions used in our measurements and covered by one CVF resolution element $\lambda/\Delta\lambda \sim 60$ each are shaded.

Our identifications of possible W-R stars agree with previous measurements, but they also reveal some additional information. We detect strong He II emission from the components R136a1, R136a2, R136a3, R136a5, and Mk 34 (outside Fig. 10), indicating luminous WNE-type stars, or, as in the case of R136a5 (Heap et al. 1994), an extreme Of star in a transition between the main sequence and W-R phase. R136a7 shows very strong emission in the Brγ map but is not visible in He II, suggesting that R136a7 may be an Of-type star (Parker et al. 1995) or another W-R star of spectral type WNL. R136b and R136c appear in both maps with slightly stronger fluxes in the Brγ line map: The components R136a4, R136a8, and R136a6 do not appear in our emission-line maps and are thus probably main-sequence O stars.

We detect several stars less luminous than the individual R136a components but which also show relatively strong emission in either the He II or the Brγ line. The stars 35, 46, 48, 57, and 58 (according to the Hunter et al. list) appear in both maps but with different intensities: e.g., the flux of star 48 relative to star 46 is significantly larger in the He II map compared to Brγ. Unfortunately, the spectral resolution (and thus the signal-to-noise ratio) in our maps is too low to identify their spectral nature reliably. However, they will be interesting targets for subsequent spectroscopic observations with Fabry-Perot interferometry.

4.2.2. *The "Red" Sources: Embedded Young Stars on the Way to the Main Sequence*

Several red supergiants were found in the surrounding 30 Doradus region (Hyland et al. 1992), indicating that star formation began there at least 10–12 Myr ago (Melnick 1992). Are there red supergiants in R136 as well? Only stars with initial mass smaller than $\lesssim 40\ M_\odot$ become red supergiants at an age larger than $\gtrsim 5$ Myr. Any massive red supergiant in R136 should be seen readily in our NIR images. Even the luminous blue variable phase predicted by the Meynet models for stars of order 40 $M_\odot$ show $m_K \simeq$ 12–16 and should be obvious. Less massive, 15 $M_\odot$ red

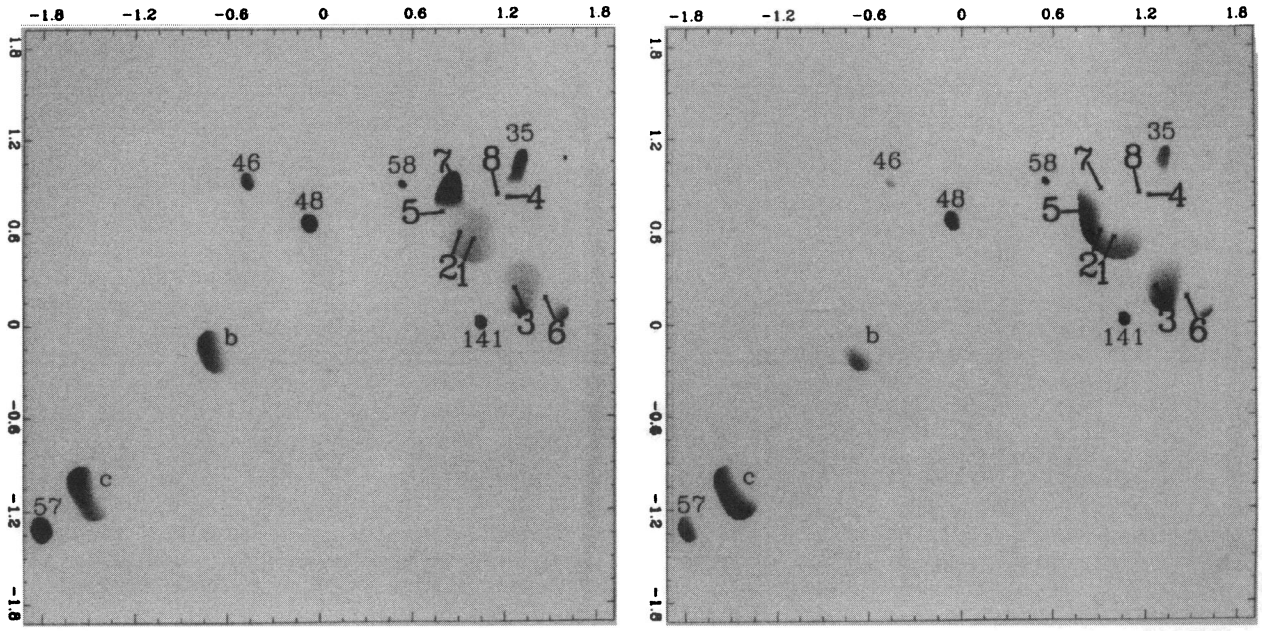

FIG. 10.—*Left*: Normalized Brγ line map of the central 4″ × 4″, taken with the SHARP II CVF. *Right*: Normalized He II line map of the same region. Both maps were continuum subtracted and normalized to the nearby continuum intensity to derive the equivalent width of the spectral line flux. The linear gray scale represents the flux intensity and allows comparisons between the individual components. The initially higher spatial resolution was degraded to ~0.″2 in order to be less sensitive to small spatial variations between continuum and line channel. The big bold-faced numbers indicate the positions of the central components R136a1–8; the smaller numbers indicate the star's numbers in the Hunter et al. list.

supergiants have $m_K \approx 11.9$–11.2 ($m_H \approx 12.6$–11.8), and even a 7 $M_\odot$ red supergiant has $m_K \approx 11.9$. Hence, supergiants should be amongst the brightest stars in our field. However, we do not detect any supergiants in our field of view.

We do find about 110 faint red sources with reliable photometric fluxes which could only be matched to model spectra with an extinction in excess of $A_V = 3$ mag (the shaded part in Fig. 8), or with $A_V > 2$ mag but unusually large residuals between the observed and model fluxes. Most of these sources were not detected in the *HST U* band; some were also not detected in the *V* band, and some went completely undetected by *HST*. Table 2 lists all our "red" sources with their apparent magnitudes, and Figure 11 displays several typical broadband spectra of the red sources. Their *UVIHK* magnitudes steadily decrease toward longer wavelengths. Since for an unreddened ZAMS 2 $M_\odot$ star, the band spectrum would be flat at approximately 1.5 mag, the red sources cannot be late-type stars but are either late-type foreground stars, strongly extincted massive stars, red giants, or cold, luminous pre–main-sequence stars with a possible infrared excess.

We estimated the number of field stars not belonging to the 30 Doradus starburst. At the galactic latitude of $b = -31°$, the probability of finding at least one galactic foreground star in our field of view is only 8% (Allen 1976). In order to include LMC field stars, we checked the star density on ESO Schmidt plates in the vicinity of the 30 Doradus cluster. The sensitivity of the *V*-band Schmidt plates is sufficient (West 1995) to detect all main-sequence stars with masses large enough to evolve into red giants with *K* magnitudes typical of our "very red" sources. This provides an upper limit on the possible contamination of our "red" sources due to red giant field stars. From the plates, we found that the probability of at least one star in our field (including the galactic foreground stars) is only ~37%. Furthermore, the probability that a contaminating field star will actually be a red giant is typically 0.25, so that the total probability of finding a contaminating red giant star in our field is $0.25 \times 0.37 = 0.09$. Hence, the chances that a significant number of the red sources are foreground or background stars is negligible.

Figure 11 shows the spatial distribution of the red sources, showing that the red sources are spread throughout our field and appear to follow the overall cluster stellar density profile, which indicates also that they are indeed members of R136.

Small-scale clumping of dusty gas in or in front of R136 could lead to a strong extinction and extreme reddening of some cluster stars. Since we do find normal extinction stars very near some of the red sources, this gas clumping would need to be on a scale smaller than ~0.″4, or 0.1 pc, with fairly high gas column densities. However, such a level of extinction should also be observed for some of the brighter objects, not just for those with $M_K > -3$. There are 400 other stars in our field with $M_K > -3$ and ~110 with $M_K < -3$, but no "red" source with $M_K < -3$. This excludes the possibility of clumpy foreground extinction, which should not discriminate between bright and faint stars. The red sources cannot be red giants within the cluster, as red giants of these magnitudes would correspond to very old stars (>350 Myr). The 30 Doradus cluster is already known to be a young region in which the oldest stars have ages of only 10–12 Myr (Melnick 1992).

The most attractive interpretation is the possibility that the red sources are young, low- or intermediate-mass PMS stars, which are still embedded in dense circumstellar gas or have significant infrared excess emission from circumstellar disks. Solar metallicity stars with masses below 5 $M_\odot$ do need several Myr to reach the main sequence, and in the solar neighborhood, solar mass young stellar objects show IR excess emission from their disks up to ages of order 10 Myr. In fact, even in 30 Doradus, several protostellar objects were recently found: knots of infrared emission, and

TABLE 2

RED SOURCES WITHIN OUR FIELD OF VIEW[a]

#	x	y	U	V	I	H	K	#	x	y	U	V	I	H	K
814	458	97	19.33	19.01	18.21	17.08	15.78	2765	385	445	—	22.96	21.56	19.45	18.52
938	481	199	18.99	19.29	18.70	16.74	16.42	2772	215	115	—	22.98	21.28	19.45	18.90
1027	261	57	20.22	19.48	18.81	17.43	16.65	2796	72	152	—	23.09	21.34	18.87	18.39
1075	499	352	20.85	19.58	18.62	—	—	2817	254	194	—	23.15	21.33	20.25	19.10
1095	423	445	20.41	19.62	18.90	17.17	16.47	2818	394	290	—	23.15	21.99	19.30	19.17
1175	279	84	20.20	19.79	19.05	17.67	16.91	2866	283	291	—	23.37	21.64	19.58	18.79
1196	383	193	20.18	19.83	18.99	17.50	16.52	2884	409	250	—	23.45	22.05	—	18.92
1245	97	293	20.62	19.92	19.24	18.16	17.15	2902	277	295	—	23.53	21.67	20.08	19.70
1277	344	136	—	19.99	19.44	16.53	16.18	2926	492	439	—	23.66	22.25	19.58	18.39
1469	320	111	—	20.36	19.01	17.32	16.94	2947	353	251	—	23.75	22.05	20.30	—
1485	305	99	—	20.37	19.53	17.70	17.00	3034	281	134	—	—	19.58	16.83	16.36
1500	249	149	21.27	20.39	19.73	17.98	17.18	3043	349	128	—	—	19.74	19.80	18.11
1530	483	443	20.09	20.43	19.65	18.03	17.67	3050	419	145	—	—	19.95	18.19	17.67
1617	492	144	—	20.57	19.22	17.00	16.81	3075	433	175	—	—	20.53	18.47	17.89
1667	295	73	—	20.65	19.95	18.57	17.41	3097	150	72	—	—	20.95	19.47	18.14
1697	473	148	—	20.69	19.88	18.22	16.97	3114	154	96	—	—	21.10	20.43	18.16
1731	199	429	—	20.74	19.34	17.32	16.83	3206	440	286	—	—	21.72	19.20	19.38
1747	216	257	—	20.77	19.49	17.99	17.67	3217	189	33	—	—	21.78	19.15	18.89
1822	238	274	—	20.90	20.10	18.76	17.97	3228	441	335	—	—	21.83	19.38	18.70
1824	408	242	—	20.90	—	19.69	18.42	3237	225	249	—	—	21.86	19.83	19.24
1934	240	393	—	21.06	19.48	17.46	17.21	3246	332	308	—	—	21.90	19.88	20.00
1991	361	301	—	21.15	20.40	18.51	17.90	3261	269	110	—	—	21.96	19.09	18.27
2003	281	37	—	21.17	19.68	17.84	17.37	3278	380	311	—	—	22.01	17.49	17.17
2025	237	471	—	21.21	19.97	18.30	17.99	3317	431	431	—	—	22.18	19.86	19.40
2033	201	60	—	21.21	19.09	16.56	16.34	3319	351	369	—	—	22.19	19.90	18.99
2036	402	344	—	21.22	19.95	18.38	18.17	3322	308	303	—	—	22.19	19.94	19.39
2046	424	340	—	21.23	20.00	18.23	17.34	3386	291	268	—	—	22.41	19.67	18.91
2090	469	198	—	21.31	19.73	18.70	18.23	3466	224	66	—	—	22.76	23.04	19.72
2095	456	347	—	21.32	19.97	18.33	18.00	9912	139	175	—	—	—	19.26	18.52
2157	373	239	—	21.41	—	18.42	18.35	9915	271	169	—	—	—	22.56	18.90
2169	157	92	—	21.42	20.18	18.19	18.39	9917	288	30	—	—	—	19.07	19.48
2239	340	295	—	21.58	20.21	18.50	18.31	9919	328	226	—	—	—	20.80	18.39
2275	58	266	—	21.65	20.19	18.78	17.89	9920	329	347	—	—	—	19.22	18.97
2313	331	254	—	21.71	20.34	18.27	17.98	9924	354	223	—	—	—	19.53	18.70
2347	218	84	—	21.79	20.42	18.23	18.15	9931	372	197	—	—	—	19.87	18.37
2350	412	351	—	21.79	20.17	18.41	18.27	9932	373	205	—	—	—	19.09	17.94
2378	145	209	—	21.84	20.37	18.53	18.57	9934	378	179	—	—	—	23.19	19.38
2412	282	93	—	21.92	20.37	18.27	17.94	9935	380	157	—	—	—	17.72	16.65
2420	436	155	—	21.95	20.65	18.19	17.20	9937	401	210	—	—	—	18.94	19.05
2470	451	162	—	22.06	—	18.72	18.73	9939	413	226	—	—	—	17.96	16.74
2490	59	293	—	22.11	20.71	18.89	18.66	9941	418	258	—	—	—	19.86	19.22
2506	299	265	—	22.16	21.33	19.29	18.54	9942	420	151	—	—	—	18.87	17.09
2520	144	17	—	22.20	20.58	19.26	—	9943	421	85	—	—	—	17.32	17.14
2528	240	286	—	22.23	20.63	18.71	18.46	9944	423	198	—	—	—	21.33	19.30
2534	225	154	—	22.23	20.59	18.48	18.11	9946	433	144	—	—	—	19.39	17.46
2602	126	289	—	22.43	20.80	18.52	17.87	9953	450	453	—	—	—	19.59	19.40
2611	342	251	—	22.46	20.78	19.04	18.81	9958	460	127	—	—	—	19.60	17.39
2627	387	395	—	22.52	21.23	18.95	18.32	9960	474	251	—	—	—	18.05	17.66
2637	385	253	—	22.54	—	18.95	17.69	9961	485	240	—	—	—	19.47	17.90
2657	251	48	—	22.63	21.10	18.98	18.55	9963	493	260	—	—	—	19.51	18.26
2672	254	51	—	22.65	21.11	19.10	18.74	9964	495	80	—	—	—	16.76	17.29
2692	247	170	—	22.71	21.40	20.21	21.40	9965	495	130	—	—	—	17.50	17.35
2720	219	262	—	22.81	20.97	19.71	19.35	9966	497	66	—	—	—	16.07	16.20
2763	161	253	—	22.96	21.03	18.85	19.24	9967	497	233	—	—	—	17.05	18.17

[a] The 108 red sources, probably pre–main-sequence YSOs, within our field of view. The first column contains the identification number given by Hunter et al. 1995; numbers >9000 are previously unknown sources. A blank line indicates that there has been no reliable detection in this particular band. We also give the *x* and *y* pixel coordinates and the apparent *UVIHK* magnitudes without corrections.

candidate protostars with masses of 15–20 $M_\odot$, one only 40″ west of R136 (Hyland et al. 1992; Rubio; Roth, & García 1992). Unless the lower mass cutoff of the IMF is above several $M_\odot$, we should in fact expect to find many evolving PMS stars. We plan to investigate the nature of our red sources in subsequent polarimetric observations.

4.2.3. *The OB Stars*

Excluding the W-R stars and PMS candidates, we derived the properties of the remaining stars by comparing their observed multiband luminosities with our models. Table 3 contains the measured *UVIHK* magnitudes of the

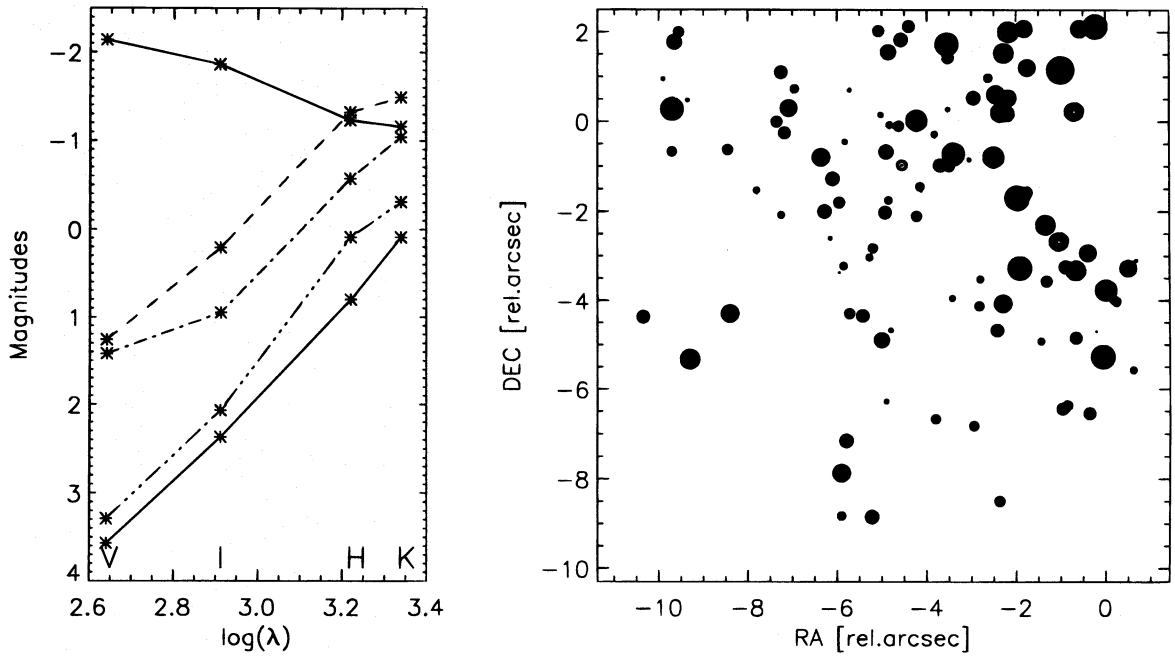

FIG. 11.—*Left*: Typical broadband spectra of four red objects with decreasing magnitudes toward longer wavelengths. For comparison, we show also the spectrum of a faint, blue B star (*top curve*). *Right*: The spatial distribution of the red sources follows the cluster profile. The size of the dots corresponds to the absolute K-band luminosity: the biggest dot is $M_K = -3$ mag, the smallest $M_K = 1.3$. The apparent lack of red sources in the very center can be explained by the position-dependent detection limit, which is smallest in the center. The red sources in general are not very luminous and, if there are any at all, they may therefore remain undetected.

TABLE 3

MAGNITUDES OF THE 25 BRIGHTEST MAIN-SEQUENCE STARS IN OUR FIELD OF VIEW

Number	x	y	U	V	I	H	K
30	432	44	13.39	14.26	14.02	13.93	14.18
31	351	76	13.44	14.35	14.08	13.66	14.48
35	434	32	13.65	14.42	14.27	13.98	14.18
36	415	115	13.66	14.43	13.98	13.34	13.40
39	487	59	13.61	14.53	14.31	13.99	14.07
40	479	72	13.62	14.54	14.35	13.93	14.10
45	398	151	13.81	14.62	14.31	13.96	14.00
46	428	121	13.94	14.67	14.26	13.73	13.79
47	454	110	13.94	14.69	14.31	13.76	13.71
48	415	103	13.91	14.72	14.37	14.01	13.92
49	475	51	13.85	14.74	14.53	14.24	14.22
50	398	82	13.92	14.75	14.48	14.00	13.95
52	369	65	13.82	14.76	14.55	14.18	14.00
55	345	82	13.92	14.80	14.53	14.15	14.21
57	325	180	14.33	14.81	14.23	13.24	12.98
58	425	77	13.95	14.82	14.55	14.23	14.03
59	385	224	14.11	14.82	14.35	13.74	13.66
62	385	55	14.02	14.96	14.75	14.60	15.10
64	489	110	14.31	15.06	14.68	14.29	14.26
65	397	144	14.33	15.12	14.49	13.98	13.77
66	393	65	14.25	15.13	14.88	14.63	14.88
68	462	228	14.43	15.16	14.76	14.22	14.15
69	385	90	14.32	15.16	15.03	14.51	14.42
71	333	56	14.31	15.17	15.00	14.55	14.52
77	365	75	14.27	15.24	14.99	14.86	15.49

NOTES.—The entire list contains ~1000 stars, except YSO candidates and W-R stars which were included in separate lists. The columns are the Hunter et al. star number, the relative x and y coordinates on our detector but on a 512 × 512 pixel subgrid, and the measured *UVIHK* magnitudes. The WFPC2 magnitudes were converted to ground-based *UVI* magnitudes according to the relations in Hunter et al. The entire list will be available on CD-ROM.

25 brightest main-sequence stars in our field of view. (Table 3 appears in its entirety in computer-readable form in the AAS CD-ROM Series, Vol. 7.) We minimized the differences between measured and model magnitudes by varying the foreground extinction, stellar age (with the constraint $t < 7$ Myr), and ZAMS mass. The minimum total difference then yields an estimate for each star's reddening, initial mass, present-day mass, age, effective temperature, and bolometric luminosity.[2] Stars that were detected in only one or two bands were fitted with a fixed extinction of $A_V = 1.57$, which is the median in our field. Table 4 lists the spectral classification of 1000 stars. Stars detected only in U and V correspond mostly to B and A types. No completeness correction factor has been applied to the shown numbers. Our detection limit reaches luminosities corresponding to ZAMS stars of a few $M_\odot$, or sub–stellar mass PMS stars, though we have not modeled PMS stars in detail for lack of reliable evolutionary models. Therefore, the "red" sources are not included in Table 4; if ZAMS masses were fitted with high extinction values, then the red sources would belong to spectral types B1 V and later.

We compare the stellar colors (Fig. 12) with theoretical evolution tracks after correcting the observed magnitudes for extinction. Note that our model fits minimize the residual between observed magnitudes and model magnitudes in a five-dimensional *UVIHK* space, whereas each color-magnitude diagram (CMD) represents only a two-dimensional projection of this space. Thus, in such a color-magnitude diagram, the stars' correspondence with the

[2] The complete computer-readable list can be obtained from the authors upon request.

TABLE 4

NUMBER OF STARS DERIVED FOR EACH SPECTRAL SUBTYPE FROM 1000 FITTED SOURCES

Mass ($M_\odot$)	Spectral Type	Total Number
.....	WN	8
120.....	O3 V	5
85.....	O4 V	8
60.....	O5 V	14
40.....	O6–7 V	19
25.....	O8 V	52
20.....	O9 V	29
15.....	B0.5 V	55
12.....	B1 V	73
10.....	B1.5 V	62
9.....	B2 V	48
8.....	B3 V	47
7.....	B4 V	57
6.....	B5 V	68
5.....	B6–7 V	76
4.....	B8 V	89
3.....	A0 V	223
2.....	A5 V and later	75

theoretical evolution tracks do not appear as convincing as if they were seen in the full five-dimensional magnitude space. However, the latter is impractical to visualize.

Most of the stars that we do not have data for in all five bands are of low luminosity and therefore lie in a region of the CMD in which the intrinsic scatter due to luminosity evolution is significantly smaller than in the regions populated by rapidly evolving massive stars.

4.3. *Cluster Age*

Although we determined ages for each star individually, we can constrain the cluster age simply from the presence of W-R stars, which indicates that star formation must have commenced at least 3 Myr ago. An upper age limit comes from the lack of red supergiants, which indicates that 40 $M_\odot$ stars probably have not entered their luminous blue variable (LBV) phase, and $\sim 30\ M_\odot$ stars have not entered their pronounced red supergiant phase. Indeed, our derived age distribution (Fig. 13) does show a clear decline of stars with age estimates larger than 4 Myr. The peak near 0 Myr is an artifact of the discrete mass binning (see § 3.5). Could star formation have commenced 4 Myr ago and continued until very recently, as suggested by our age distribution?

An intriguing method to constrain the age and duration of a starburst is the analysis of the relative abundance of W-R and O stars. The minimum ZAMS mass of a star with a final W-R phase (with enhanced mass loss and $Z = 0.008$) is $\sim 35\ M_\odot$, and its lifetime is about 5.5 Myr, of which the W-R phase lasts for 0.5 Myr (Meynet et al. 1994; Maeder & Meynet 1993). Stars with $m_0 > 15\ M_\odot$ are considered O stars. The quoted mass range and duration of the W-R phase depend on the stellar mass loss, which is not well understood. Ignoring the uncertainty introduced by a poorly constrained stellar mass-loss evolution, the ratio of W-R to O stars then depends on the shape of the IMF above 15 $M_\odot$, as well as the beginning and the duration of the star burst.

From *HST* photometric data, Parker et al. (1995) estimated a W-R to O star ratio of 0.11 ± 0.03 in R136, which they could match with a model of high–mass-loss stars, a

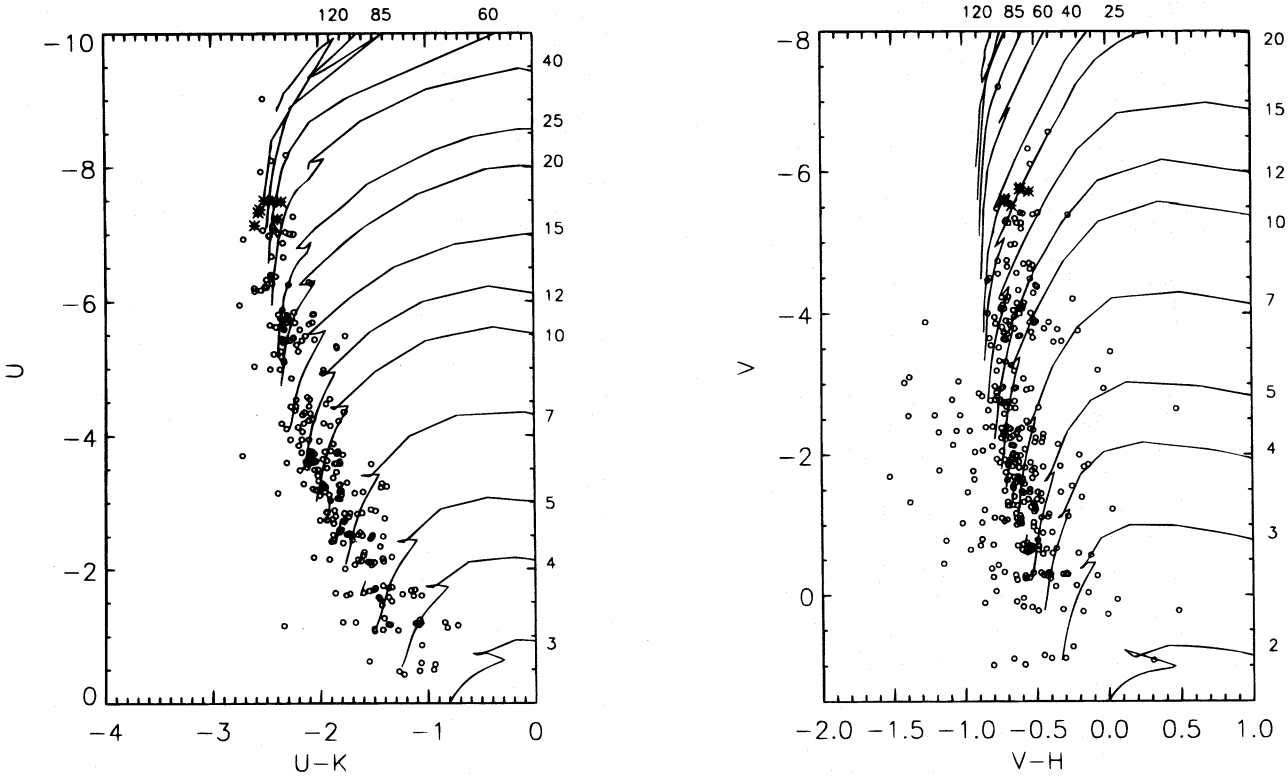

FIG. 12.—Color-magnitude diagrams from the reddening-corrected observed band luminosities (*open circles*). Theoretical evolution tracks for most mass bins are shown as lines labeled by their corresponding mass. The differences between the two diagrams illustrate the uncertainties when using only two or three wave bands for identification. Asterisks indicate the sources fitted as $85\ M_\odot$ stars. W-R stars and red PMS candidates are not plotted.

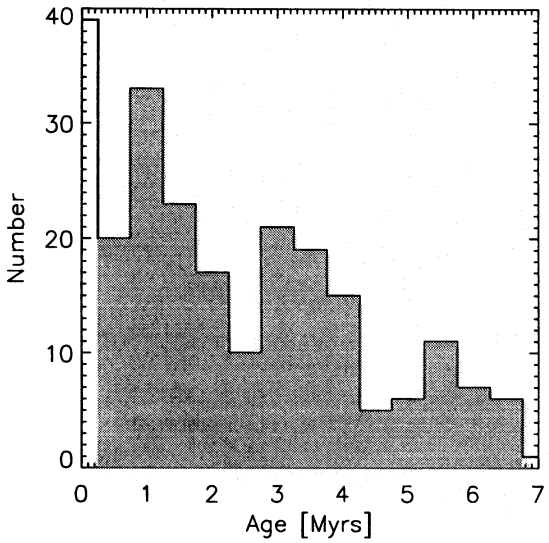

FIG. 13.—Stellar age distribution from the model fits for stars more massive than 12 $M_\odot$. The peak near 0 Myr is an artifact of the discrete mass binning. The possible ages in the fit were restricted to 0–7 Myr.

shallow IMF ($\Gamma \approx -1$) with a high upper mass cutoff ($m_{up} > 80\ M_\odot$), and a short burst ($\Delta t < 1$ Myr) ~3.5 Myr ago. However, calculating the W-R/O star ratio for R136 may be biased by an unusually high concentration of W-R stars at radial distances of 8″–14″ from the cluster center. This "ringlike" structure includes the known and candidate Wolf-Rayet stars Mk 33S, Mk 34, Mk 35, Mk 37, Mk 37W, Mk 39, Mk 42, and R134. The "ringlike" concentration of the most massive stars leads to a hump in the radial surface mass density profile as observed by Malumuth & Heap (1994, Fig. 13). Assuming an IMF slope $\Gamma = -1.6$ for this region (see § 4.4.3), we would expect many more massive O stars than observed by the *HST*.

Whether or not these W-R stars belong to the starburst in R136 cannot be determined unambiguously from our data. On average, massive stars tend to settle toward the cluster center, but due to close encounters with other massive stars or binaries even the most massive stars can be ejected into the cluster outskirts. However, we know of no dynamical mechanism that would selectively eject about 50% of the total number of W-R stars in the entire region, but not the other massive O stars. Therefore, we assume that the outer W-R stars are not related to the central starburst.

Hence, we adopt a W-R/O star ratio that includes all known W-R stars within our field of view (R136a1, R136a2, R136a3, R136c, Mk 34) as well as stars that are believed to be in a transition phase between O and W-R star (R136a5, R136a7, R136b). We find $\text{W-R/O}_{fov} = 8/127 = 0.06$, a value unaffected by mass classifications derived from the age-restricted fit as described in § 3.5.

The W-R/O ratio of our full field may be biased, as it includes the entire core of the cluster but only about one-quarter of the surrounding region. Therefore, we calculated the W-R/O ratio in a circular region around R136a1. Since we have no information on the O star population outside our field of view, we restrict our W-R/O analysis to the region within a radius of 7″. This value is large enough to cover the R136 region entirely, but it should not be affected by the "ring" of W-R stars further out. Seven W-R stars (all the stars listed above, with the exception of Mk 34) are known within 7″. In order to derive the number of O stars, we take their number in our field of view for the outer parts, multiply by four assuming radial symmetry, and add this number to the value derived form the central cluster (which is entirely within our observed field). Then we find $\text{W-R/O}_{[r \le 7'']} \approx 7/187 = 0.04$.

Both estimates are in good agreement, indicating a relatively low ratio of W-R/O ≈ 0.05. This value would be expected for a cluster age of ~3.5 Myr (Parker et al. 1995, Fig. 6), assuming twice-enhanced mass loss (as observed by Heap et al. 1994), an upper mass limit of 120 $M_\odot$, and an IMF slope of $\Gamma \sim -1.6$ (as derived in § 4.4.3). Given the age of ~3.5 Myr, W-R/O ≈ 0.05 also suggests a relatively short duration of the starburst ($t_{sb} \ll 1$ Myr) rather than continuous, ongoing star formation (Parker et al. 1995, Fig. 7).

4.4. *The Stellar Mass Function*

The initial mass function (IMF) describes the stellar mass distribution at birth, $\xi(m)$. Constraining its shape and mass range in a massive starburst region is one of the foremost challenges in modern astronomy. Starbursts play an important role in the star formation history and evolution of galaxies, as they can alter dramatically their color, luminosity, and morphology. In a starburst galaxy, the star formation rate can be inferred indirectly from, e.g., the total IR or Brγ luminosity. If most of the stellar radiation is absorbed by dust and reradiated at IR wavelengths, the total IR luminosity is an approximate measure of the stellar content. On the other hand, the luminosity of the hydrogen recombination lines provides a measure for the total ionizing radiation luminosity. In either case, the measured luminosities are dominated by the most massive stars, which comprise only a small fraction of the total stellar mass. Estimates of the total star mass thus depend critically on the shape and range of the IMF.

Sudden bursts of star formation may have an IMF that differs from that in regions of "quiescent" star formation. A detailed study of the IMF in starburst regions may reveal crucial insights into the different modes and processes that regulate star formation. R136 provides a unique opportunity to study a starburst IMF in detail, as it is the only massive starburst near enough to allow for a direct measurement of the IMF through the identification of individual stars.

For simplicity, the IMF is often fitted by a power law with constant slope at intermediate and high mass:

$$\xi(\log m) d \log m \propto m^{\Gamma}\, d \log m\ ; \qquad (4.1)$$

at low mass, $m \lesssim 0.5\ M_\odot$, the IMF is generally observed to level off. In general, $\Gamma = \Gamma(m) = \partial \log \xi(m)/\partial \log m$. Stars may only form between a lower mass, m_{low}, and a maximum, m_{up}, beyond which Γ drops significantly.

Since massive stars are much brighter, m_{up} is more easily measurable, provided that there are sufficient numbers of stars to measure a statistically significant drop of Γ. For small clusters, the number of stars may drop to zero at intermediate stellar masses, so that a determination of a real IMF cutoff is not possible. In massive clusters that are older than 2–3 Myr, the most massive stars are increasingly depleted as they turn into W-R stars (for which an accurate initial mass determination is nearly impossible) and die shortly afterward in supernova explosions. Here the observed mass function, usually referred to as the "present-day mass function" (PDMF), differs from the IMF, and a determination of the latter is possible only up to the mass of

a star whose lifetime equals the age of the cluster. The shape of the IMF at low masses and the lower mass cutoff are also difficult to constrain, especially for distant, dense star clusters like R136. Studies in the solar neighborhood indicate that $m_{low} \simeq 0.1\ M_\odot$.

Early studies of the IMF in our galaxy found $\Gamma = -1.35$ (Salpeter 1955) at intermediate masses. Miller & Scalo (1979) found $\Gamma = -1.5$ in the mass range 1–10 $M_\odot$. Recent studies show, however, that Γ may vary substantially from region to region. An emerging trend is that regions with a high star formation rate (such as OB associations) somewhat favor the production of more massive ($m > 15\ M_\odot$) stars. Outside 30 Doradus, Massey et al. (1989) found $\Gamma = -1.8 \pm 0.1$ for the OB associations LH 117 and LH 118. In 30 Doradus, $\Gamma = -108 \pm 0.2$ for the massive stars in LH associations (Hill et al. 1994), while the entire region has $\Gamma = -1.5 \pm 0.2$ (Parker & Garmany 1993).

Using our mass determinations of ~1000 stars in R136, we are in a position to not only determine the cluster's average high- and intermediate-mass IMF, but also to measure radial variations in the IMF slope that may be due to the cluster's dynamical evolution.

4.4.1. *Previous IMF Determinations in R136*

Previous investigators have examined the IMF slope in R136 with apparently conflicting results: Malumuth & Heap (1994) calculated the mass of each star from the measured B magnitude at $B = 12.5$–16.5 mag, i.e., for stars more massive than ~20 $M_\odot$, using the spectral synthesis program CLUSTMOD and assuming a cluster age of 3 Myr. Excluding the W-R stars, they derived $\Gamma = -0.90 \pm 0.38$ inside the central $3''.3 \times 3''.3$ and $\Gamma = -1.82 \pm 0.41$ outside. On the other hand, Hunter et al. (1995) determined individual stellar masses from the dereddened WFPC2 colors and isochrones for a cluster age of 4 Myr. With six mass bins from 2.8 to 15 $M_\odot$, they derived $\Gamma = -1.2 \pm 0.1$ and found no significant variation with radial distances between 0.5 pc and 4.7 pc, and hence no evidence for mass segregation beyond 0.5 pc.

4.4.2. *Completeness*

In order to derive the PDMF for all stars in our sample, we have to take into account that a significant number of stars may have remained undetected due to crowding. Especially in the cluster core, many stars with luminosities above the detection limit for isolated sources remain undetected because they are obscured by nearby, brighter objects. Hence, we introduce a completeness correction factor (CCF) that is multiplied with the observed quantities (number counts, total mass, etc.) to obtain a correction estimate for their true values. Since incompleteness is in general a function of the source position, brightness, and observed wavelength, the CCF must be derived for several luminosity and radial bins. This is usually done by adding artificial sources to the observed image and a subsequent determination of the percentage of redetected sources. Since the maximum spatial resolution is proportional to the wavelength, and since crowding is more severe for lower resolution images, one would expect larger correction factors at longer wavelengths for similar sensitivities at all wavelengths. Hunter et al. (1995) calculated and published the CCFs for their F555W and F814W images (their Table 4) and demonstrated a general trend of increasing CCF with increasing wavelength. Because of the good agreement between our NIR and the *HST* observations, and since the total number of sources in our combined multicolor sample is based on the *HST* counts anyway, we may also apply the Hunter et al. CCFs in our analysis. This means that we cannot correct properly the observed number of sources which appear only in the NIR bands. However, these sources (as we have discussed in § 4.2.2) generally show large reddening, and their mass estimates are so uncertain that they were excluded from the cluster mass mass profile anyway.

4.4.3. *Mass Segregation*

W-R stars form the final short (~500,000 yr) epoch in the life of stars with mass in excess of ~40 $M_\odot$. W-R stars are the brightest NIR sources in R136, and we notice a high relative abundance of them in the very center of the cluster. From the Meynet et al. (1994) evolution tracks, it appears that a star in its W-R phase is at an age (depending on its initial mass) between 2.8 and 5.5 Myr, the upper limit being somewhat uncertain because it derives from an interpolation between Meynet's evolutionary tracks. Since the W-R phase is short and limited to a narrow stellar mass range, the local density ratio between W-R stars and O stars varies substantially with time and depends strongly on Γ, m_{up}, and the duration of the starburst (Parker et al. 1995). The high W-R/O star ratio of (5/29) in the central 1″ of R136 is striking evidence for strong mass segregation and a short starburst duration. This ratio is several times larger than what would be expected from an unsegregated IMF with normal Salpeter IMF and an instantaneous burst 3 Myr ago.

Another indication for mass segregation comes from the variation of the PDMF slope with distance from the cluster center. For our entire field of view, we find $\Gamma = -1.59 \pm 0.10$ (Fig. 14). However, for $r \leq 0.4$ pc we find $\Gamma = -1.33 \pm 0.16$, and for $0.4 < r \leq 0.8$ pc, we find $\Gamma = -1.63 \pm 0.18$. For $r > 0.8$ pc, we find that a single power law does not fit the distribution very well, so we derived separate slopes for the higher ($m > 12\ M_\odot$) and intermediate ($m < 25\ M_\odot$) mass ranges. In the upper range, $\Gamma = -2.16 \pm 0.29$, indicating a strong deficiency of high-mass stars, while the lower mass range, $\Gamma = -1.52 \pm 0.09$, is similar to the value of $\Gamma = -1.5$ measured by Parker & Garmany (1993) on a larger scale in the 30 Doradus region. The error bins in Figure 14 include the statistical (Poisson) errors, the errors from the completeness correction (given in Hunter et al.'s Table 4), and a 30% error on the individual mass determination.

As described in § 3.5, restricting the burst age spread improves the accuracy of the mass determination, but with a loss of generality. Hence, we recalculated the slope for our sample of stars, allowing only ages between 2.5–3.5 Myr (see Fig. 7). For our entire field of view, we find $\Gamma = -1.57 \pm 0.10$. Separated in different radial bins, we find $\Gamma = -1.29 \pm 0.20$ ($r \leq 0.4$ pc), $\Gamma = -1.46 \pm 0.23$ ($0.4 < r \leq 0.8$ pc), and $\Gamma = -2.12 \pm 0.09$ ($r > 0.8$ pc). The slopes derived this way are almost identical to the ones determined from the more general fit. The smaller difference illustrates the reliability of our fit procedure for the determined mass spectrum of the cluster.

We have also investigated the effect of a fixed mean reddening of $A_V = 1.55$ (instead of individual extinction as a free fit parameter) to the derived mass function. The average slope for all stars in our field is not affected significantly; the slope for the central region flattens from $\Gamma = -1.33$ to

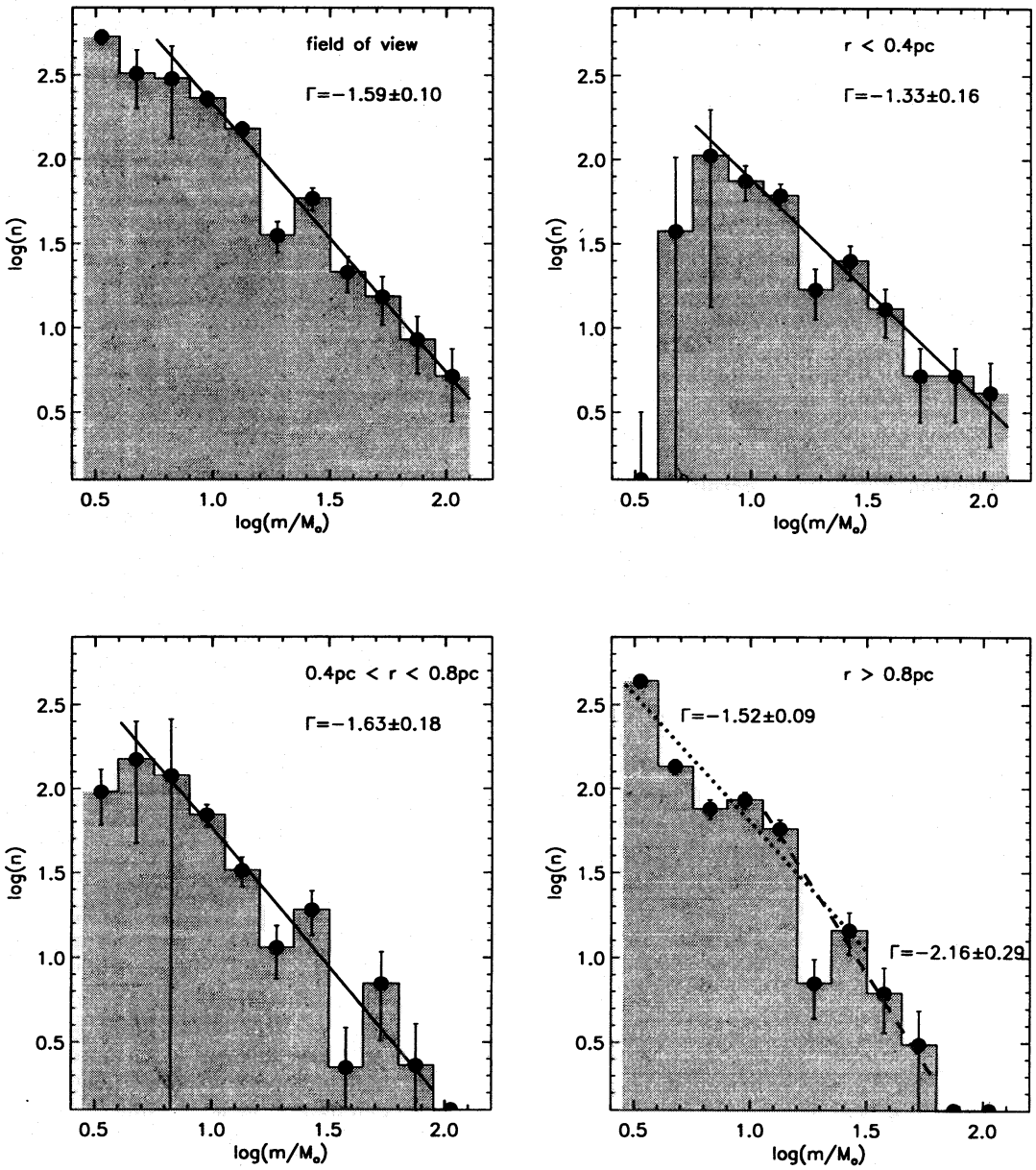

FIG. 14.—Slope of the mass function for stars in our entire field of view and three different radial bins, corrected for completeness. The slope in the entire field is $\Gamma = -1.59 \pm 0.10$. For $r \leq 0.4$ pc, $\Gamma = -1.33 \pm 0.16$, for $0.4 < r \leq 0.8$ pc, $\Gamma = -1.63 \pm 0.18$, and for $r > 0.8$ pc, $\Gamma = -1.52 \pm 0.09$ (for $m < 25\,M_{\odot}$) and $\Gamma = -2.16 \pm 0.29$ (for $m > 12\,M_{\odot}$). The lines show linear fits to the data; the length of the lines corresponds to the fitted mass range. The error bars include the statistical (Poisson) errors, the errors from completeness correction and a 30% error on the individual mass determination. W-R stars and "red" objects were excluded for reasons also described in the text.

$\Gamma = -1.26$, whereas outside 0.8 pc the slope for both intermediate- and high-mass stars becomes steeper: $\Gamma = -1.52$ to $\Gamma = -1.83$ and $\Gamma = -2.16$ to $\Gamma = -2.62$, respectively. Hence, neglecting the individual stellar extinction strengthens the differences in the slope between inner and outer regions and may lead to overestimating the mass segregation.

Thus, both from the high abundance of W-R stars and from the variation of Γ we see clearly that the mass distribution in the center of R136 is weighted toward more massive stars. This may be due to a spatially variable IMF—more massive stars were born toward the center and stayed there—or it may be the result of dynamical processes that segregated an initially spatially uniform mass distribution. We cannot disprove the first option; however, a quantitatively dynamical analysis shows that strong mass segregation must surely have taken place in R136.

4.5. *The Dynamical Evolution of R136*

4.5.1. *The Core Radius of R136*

If a star cluster is in near-thermodynamic equilibrium (clusters can never be in complete equilibrium, or they would require infinite mass), it consists of an isothermal core with radius r_c surrounded by a tidally truncated halo of radius r_t. Its projected profile is described observationally by a King (1962) distribution:

$$I(r) = I_0\left[\frac{1}{\sqrt{1+\left(\frac{r}{r_c}\right)^2}} - \frac{1}{\sqrt{1+\left(\frac{r_t}{r_c}\right)^2}}\right]^2 . \quad (4.2)$$

The core radius is the distance at which two-dimensional quantities (e.g., star counts, luminosity or mass distribution) fall to half of their central value, $I(r_c) = I_0/2$. The core radius may also be expressed in physical terms (Spitzer 1987):

$$r_c = \sqrt{\frac{3\sigma_0^2}{4\pi G\rho_0}}, \tag{4.3}$$

where σ_0 is the central, radial velocity dispersion and ρ_0 is the central mass density. The values of r_c derived from observations of the quantity $I(r)$ and via σ_0 and ρ_0 are equal to within $\approx 10\%$ for clusters with $r_t/r_c \geq 10$ (Lightman & Shapiro 1978). To first order, cluster dynamics are governed solely by the core radius; hence, we begin our dynamical discussion with a presentation of r_c derived from our observations.

The mass determination from our fit permits us, within the limits of completeness, to make true density profiles of the cluster, to which we fit King profiles and derive core radii (Fig. 15). However, we find that stars of different masses show pronounced, systematic variations of the core radius, ranging from 0.″2 to 1.″2. This result follows naturally from the progressive increase of Γ with radius: massive stars dominate at the center, thus their "core" is smaller than that of light stars. Since the radial variability of Γ (and hence the mass dependency of r_c) is not due to incompleteness, we present, rather than a single number for the core radius, a plot of our derived values for various lower mass cutoffs ranging from our detection limit of 2 $M_\odot$ to 40 $M_\odot$ (Fig. 16). The curve begins flattening around 15 $M_\odot$, which corresponds to a main-sequence spectral type B0.5. The uncertainty in the core radius for each mass cutoff is determined in large part by the graininess of the mass distribution, which limits the accuracy of core radius determinations even in globular clusters (several thousand times older than R136), where the luminosity difference between stars dominating the mass (an M dwarf or lighter) and those dominating the luminosity is limited to a factor of 10 or so. Young clusters like R136 with many extremely luminous stars are affected even more by the granularity problem. Our methodology, which determines the mass of each star, can reduce the uncertainty in the core radius to its minimum value (Sams 1995). Misjudging the true cluster center is also a potential source of error in the core radius calculations. We evaluated this effect by shifting the nominal cluster center 0.″2 in 12 radial directions, and we found that the derived core radii varied by no more than 0.″05. In addition, subclustering of massive stars can cause significant profile irregularities such as that at $r \approx 2''$ (Fig. 15).

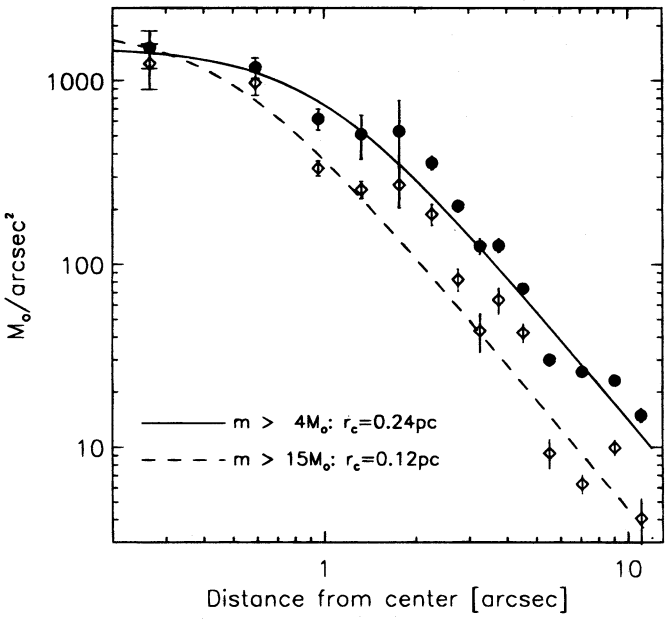

FIG. 15.—Fit to the mass density distribution of stars with $m > 4\ M_\odot$, which is the mass range that we covered by the completeness correction (*solid line*). Fitting a standard King profile yields $r_c = 0.''97 \pm 0.''07$ (0.24 pc). If we restrict the fit to stars with $m > 15\ M_\odot$, the number of stars drops significantly, but the core radius also shrinks to $r_c = 0.''48 \pm 0.''09$ (0.12 pc) (*dashed line*). Going to even higher cutoff values, a pure power-law fit yields approximately the same χ^2 as the King fit. The first data point was not included in the fit.

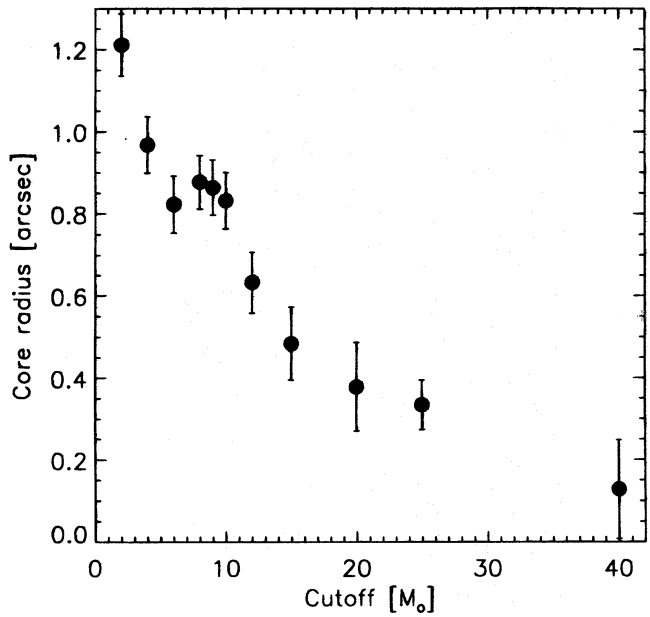

FIG. 16.—The core radius as a function of the detected mass range $r_c = f(m_{\rm limit})$. The mass density distribution was corrected for completeness; however, the first measurement ($r_c = 1.''21$) includes all determined stars and is not complete toward a lower mass cutoff. The error bars for the fit to the $m > 40\ M_\odot$ distribution are somewhat arbitrary, since this distribution is also well fit by a power law (the result of the King fit depends strongly on the start values). The reliable results in between the outer data points show a clear trend toward smaller core radii for brighter stars (i.e., less sensitive observations).

Again, we have checked the differences deriving from an age-restricted fit. For stars with, e.g., $m > 15\ M_\odot$, we find $r_c = 0.''35 \pm 0.''05$, a slightly smaller value than in the nonrestricted fit. However, the individual core radii, derived from an age-restricted fit, support the trend that the core radius depends on the observational lower mass cutoff.

Our finding that no single r_c describes R136 may also explain the discordance among previously derived core radii. Hunter et al. (1995) calculated the core radius by summing up the luminosities of all stars within a unit area at different radial distances and converting these values into total masses, assuming a mass-to-light ratio $m/L \sim 0.008$, and they found $r_c \leq 0.''08$ (0.02 pc). We consider this approach somewhat unreliable for the following two reasons. First, a few very bright W-R and O stars, which are unusually concentrated but which contribute only a few

percent of the total dynamical mass, will dominate the luminosity profile. This central peak contains most of the luminous stars and may lead to a significant underestimate of the core radius. Second, the m/L ratio depends on Γ, m_{up}, and m_{low} and evolves with time after the initial starburst. The technique of estimating m from L and the m/L ratio is not hopeless, however, as sophisticated models exist to calculate it (Bruzual & Charlot 1993). Proper application of the method requires accurate knowledge of the local PDMF and burst age, without which the uncertainties in the derived core radius may be far larger than the formal errors indicate.

In contrast, Malumuth & Heap (1994) calculated the ZAMS mass for the massive stars individually, using a spectral synthesis program and adopting a cluster age of 3 Myr, and they summed up the stellar masses per unit area as a function of the radial distance. They derive $r_c \approx 0\farcs96$ (0.24 pc), a core radius that is about 10 times larger than the measurement by Hunter et al. From the surface brightness profile at the same data, Campbell et al. (1992) calculated $r_c \leq 0\farcs25$. De Marchi et al. (1993) derived $r_c \approx 0\farcs6$ and $r_c \approx 0\farcs4$ from the light distribution in deconvolved FOC images taken in the F130M and F346 filters, respectively. Several ground-based measurements yielded core radii in the range between $r_c = 0\farcs8$ (Moffat, Seggewiss, & Shara 1985) and $r_c = 1\farcs3$ (Meylan 1993).

4.5.2. *Cluster Dynamics*

Here we study the dynamics of R136 as an isolated N-body system. This assumption is justified by the fact that r_t/r_c is large (≥ 16; Meylan 1993), so that the cluster's central regions are relatively free of gravitational tides from the LMC. Because the cluster relaxation time, t_r, is density and mass dependent and therefore varies significantly throughout the cluster, it is customary to consider the relaxation time of the entire cluster system as a whole via the half-mass relaxation time (Lightman & Shapiro 1978):

$$t_{rh} = \frac{v_{rel}^3}{15.4 G^2 \bar{m}^2 n \ln(0.4\ N)} \tag{4.4}$$

$$= 5 \times 10^8 \text{ yr } (N/5 \times 10^4)^{1/2} (\bar{m}/M_\odot)^{-1/2} (r_h/5 \text{ pc})^{3/2}\ , \tag{4.5}$$

where N is the total number of stars in the cluster, $\bar{m} = m_{tot}/N$ is the mean stellar mass, v_{rel} is the mean relative velocity between a star and its neighbors, n is the local star density, and r_h is the half-mass radius. The half-mass relaxation time is the relaxation time at the mean density for the inner half of the cluster mass, for stars having an rms velocity characteristic of the cluster as a whole. We now estimate this timescale and compare it to the time required for the population of heavy stars to evolve. If the relaxation time of high-mass stars is significantly shorter than that of the mean cluster stars, and less than or equal to the cluster age, then dynamical evolution and mass segregation could be responsible for the PDMF slope variations observed across R136.

We determine $\bar{m}$ by integrating the PDMF (using our "average" value of $\Gamma = -1.6$) over appropriate upper and lower mass ranges:

$$\bar{m} = m_{tot}/N = \frac{\int_{m_{low}}^{M_{up}} x^\Gamma\, dx}{\int_{m_{low}}^{m_{up}} x^{\Gamma-1}\, dx}\ . \tag{4.6}$$

Fortunately $\bar{m}$ is only very weakly dependent on m_{up}, and reasonable values of m_{low} varying from 0.1 to 0.3 $M_\odot$ give $\bar{m}$ varying from 0.3 to 1.0 $M_\odot$, from which we choose 0.5 $M_\odot$. The core radius for the mean cluster stars can be taken from Figure 16. Bearing in mind that the data for $m < 4\ M_\odot$ begin to become incomplete, we take $r_c = 1\farcs0$ as the effective core radius of low-mass stars. To calculate the half-mass radius from r_h, we require r_t, which has been determined by two independent investigations. Malumuth & Heap (1994) find $r_c = 1\farcs0$ with $r_t \approx 100''$ fitting well within their $17\farcs5$ radius field. Meylan (1993), on the other hand, measured the profile of R136 out to 100″ in B and V bands. In both cases, he found that the cluster profile was best fit by two distinct King profiles, a smaller profile with $r_c = 1\farcs3$ and $r_t = 21''$, which is superposed on a larger profile with $r_c = 15''$ and $r_t \approx 1500''$. The central surface density of the very large scale profile is only 1/100 that of the smaller profile, and so it plays little role in the gravitational dynamics of the central cluster. The fact that our derived core radius for low-mass stars is in agreement with that of Malumuth and Heap, as well as with the smaller one of Meylan's profiles, suggests to us that $r_t = 21''$ is a reasonable estimate for dynamical considerations of the central star cluster. Hence, we find the effective half-mass radius of R136 to be $r_h \approx 0.2 r_t$, when $r_t/r_c \approx 10$ (Spitzer 1987, p. 16), or $0.2 \times 21'' = 1.1$ pc.

To determine N, we require the total mass of the cluster within r_h, which cannot be evaluated directly because most of the mass is due to stars below our detection limit. Instead we are forced to estimate the total central mass from the observed total K luminosity and the m/L_K ratio. Current stellar evolution codes (Bruzual & Charlot 1993) predict the m/L_K ratio of a starburst as a function of time for different IMFs and mass cutoffs. Using a Salpeter IMF with $m_{low} = 0.1\ M_\odot$ and $m_{up} = 125\ M_\odot$, and a burst of age 3.5×10^6 yr, they find that 1 $M_\odot$ of stars produces 1.2 K magnitudes.

For R136, however, the actual m/L_K ratio is rather poorly constrained in part because the initial upper and lower mass cutoffs are not well known, and because their present-day values may have been altered by dynamical mass segregation (which would act to decrease m/L_K in the cluster's central regions). The uncertainty in m/L_K due to these effects can be estimated by examining m/L_K for different IMF mass cutoffs. Decreasing the upper mass cutoff to 65 rather than 125 $M_\odot$, for example, produces an m/L_K variation of 0.5 mag, while increasing the lower mass cutoff decreases the m/L_k ratio. Let us then conservatively estimate the error in m/L_k due to mass cutoffs at 1 mag. In addition, m/L_K is time dependent over the range near the expected cluster age of 3.5×10^6 yr: from 3.0×10^6 yr to 4.0×10^6 yr (roughly the age range of R136), it varies by over 1 mag. Hence, we estimate that the total uncertainty in m/L_k is ≈ 1.5 mag. Using the total measured K magnitude $K = 8.6$ and the distance modulus $D_l = 18.6$ to the LMC, this corresponds to $\sim 3 \times 10^4\ M_\odot$ of mass contained within the projected central 20″. The upper limit on this value is $1.5 \times 10^5\ M_\odot$. Our estimate lies close to the value of $1.7 \times 10^4\ M_\odot$ derived by Malumuth & Heap, but it is 25 times smaller than the $7.5 \times 10^5\ M_\odot$ derived by Campbell et al. (1992). Even given the uncertain values of m/L_k, we find the Campbell et al. value unlikely, particularly given the fact that any significant variation of the most uncertain quantity (the lower mass cutoff) acts to decrease the m/L_k ratio. Finally, we estimate the total number of stars in the central part of the

cluster to be $N = m_{\rm tot}/\bar{m} \approx 3 \times 10^4/0.5 = 6 \times 10^4$. Using the values derived above, we find $t_{\rm rh} = 7.8 \times 10^7$ yr. Taking our extreme upper limit for the number of stars in the core as 10 times larger, we derive $t_{\rm rh} = 2.5 \times 10^8$ yr as the evolutionary time for the entire cluster.

However, our finding that the core radius r_c is mass dependent already showed that mass segregation may at least partially have taken place in R136. Therefore, we estimate the time required for mass segregation under the following simple assumption. Let the cluster population consist of two mass ranges: rare, heavy stars with m_H, and common, light stars with m_L. Initially, the cluster potential will be domiated by the light stars, and if the light and heavy stars are mixed equally, then the ratio of the relaxation times for the two populations is given by (Spitzer 1987)

$$\frac{t_{rH}}{t_{rL}} \sim 0.44 \frac{m_L}{m_H} \left(1 + \frac{v_H^2}{v_L^2}\right)^{3/2}, \qquad (4.7)$$

where v_H and v_L are the mean velocities of the heavy and light stars. When $m_H/m_L \gg 1$ (i.e., $v_H^2/v_L^2 \ll 1$), thus $t_{rH}/t_{rL} \approx 0.5\, m_L/m_H$. Hence, if the W-R and O stars have $m > 20\, M_\odot$, and the mean stellar mass is $0.5\, M_\odot$, they will evolve $2m_H/m_L = 80$ times faster than the cluster as a whole. To be conservative, we choose our upper limit for $t_{rh} = 2.5 \times 10^8$ yr to be the evolutionary time for the entire cluster, and we find that the heavy stars will sink to the center in only $t_{rH} = 3 \times 10^6$ yr (if we had chosen our preferred value of $t_{rh} = 7.8 \times 10^7$ yr, the heavy star relaxation time would be $t_{rH} = 1 \times 10^6$ yr, several times smaller than the derived cluster age).

In fact, the evolution of massive stars will occur faster than these estimates because as they become more concentrated toward the center, they will interact more and more frequently with each other rather than with the light stars, and consequently they will suffer larger angle deflections more often, leading to a more rapid evolution. This is tantamount to assuming a certain amount of "preclustering" in 30 Doradus which increases dramatically the likelihood of significant mass segregation. Let us consider the half-mass relaxation time for stars in the core itself. From equation (4.4), and using a core radius of 0.1 pc (our derived value for the heavier stars) and estimating the central density from the surface brightness and m/L_K ratio to be $\approx 10^5\, M_\odot$ pc^{-3}, we find that the relaxation time for $10\, M_\odot$ stars in the core is $t_r(10\, M_\odot) \approx 10^5$ yr. Now since $t_r \propto N(r) r^{3/2} \bar{m}^{-1/2}$ and $N(r) \propto r$, then $t_r \propto r^{5/2} \bar{m}^{-1/2}$, and hence at $r = 10 r_c$ the relaxation time for the same $10\, M_\odot$ stars is $\sim 10^7$ yr.

This differentiation leading to mass segregation is an accelerating process, which tends to settle the most massive stars in the core, even as the cluster is forming. Hence, with some preclustering, the mass segregation timescale could be as short as 10^5–10^6 yr.

In any case, the relaxation time for massive stars is probably less than the cluster age, and so some dynamical relaxation is certain to have occurred. The estimates presented above are very conservative, but they show nevertheless that dynamical mass segregation must have played an important role in producing the radial variations of the PDMF. Because our derived value for the half-mass relaxation time, t_{rH}, is comparable to the cluster age, we cannot completely rule out a position-dependent IMF; however, there is no need to invoke one, either.

5. SUMMARY

Near-infrared imaging with adaptive optics is a powerful new tool for ground-based observations; it produced diffraction limited images of R136 which compare well in resolution and depth with those of *HST*. Indeed, we detect not only a representative sample of the *HST* sources, but also a new population of highly reddened sources which are most likely pre–main-sequence objects. By combining our adaptive optics observations with *HST* data, we fit stellar evolution models to the measured *UVIHK* magnitudes and derive the stellar population. As our wide wavelength coverage allows us to solve for the extinction of every individual star, rather than assigning a mean extinction to all stars, the derived stellar masses are the most accurate yet for the upper and intermediate regime of the mass function in a massive starburst.

Our most significant findings are as follows:

1. The extinction varies significantly from star to star within the cluster. Its variation has a range of 1–2 mag, which substantially affects stellar classifications based on multiband photometry.
2. We detected and confirmed the previously known WN stars by NIR emission-line observations.
3. We detected a population of at least 110 red objects (roughly half of which have not been seen previously), which are probably pre–main-sequence stars, and which are still embedded in dense circumstellar gas or show IR excess emission from circumstellar disks.
4. We found no red giants or red supergiants within our field of veiw, which constrains the age of the cluster to be less than 5 Myr.
5. An even younger age of ~ 3.5 Myr can be derived from the observed W-R/O star ratio of ≈ 0.05.
6. The average mass function within R136, $\Gamma = -1.6$, is not significantly different from the surrounding 30 Doradus region, but the slope varies slightly with distance to the cluster center.
7. The slope of the mass function plus the derived W-R/O star ratio indicate a short starburst duration, significantly less than 1 Myr.
8. The derived core radius depends strongly on the observational lower mass cutoff (i.e., the sensitivity of the observations); this may explain the contradictory results of previous observations.
9. Both mass function and core radius variations indicate strong mass segregation, which is almost certainly due to the dynamical evolution of the cluster.

Together these results comprise the most detailed study of the stellar population in a massive starburst. They suggest that the upper end of the IMF is similar to that observed locally in the Galaxy and demonstrate the important effects of dynamical evolution upon spatial variations of the PDMF. We expect that NIR adaptive optics, with high spatial resolution and dust penetrating ability, will play an ever-increasing role in future studies of starburst populations.

The authors would like to thank Eliot M. Malumuth, Sara R. Heap, and Hans Zinnecker for valuable discussions and Deidre A. Hunter for placing the WFPC2 data at our disposal before publication. The referee, Joel Wm. Parker, provided many helpful comments which improved the

manuscript greatly. He and Pat R. J. Morris also sent us prepublication data on W-R stars. We thank all involved people from ESO and Observatoire de Meudon for their support in getting our joint system running, and particularly Jean-Luc Beuzit for many fruitful discussions. We also would like to thank Richard Hook for his help in understanding and running PLUCY at the ESO facilities.

REFERENCES

Allen, C. W. 1976, Astrophysical Quantities (London: Athlone)
Bertoldi, F., & Jenkins, E. B. 1992, ApJ, 388, 495
Beuzit, J.-L., et al. 1995, in preparation
Bouchet, P., Manfroid, J., & Schnider, F. X. 1991, A&AS, 91, 409
Brandl, B. 1995a, S&T, 90, No. 2, 14
———. 1995b, Ph.D. thesis, Ludwig-Maximilians-Universität München
Brandl, B., Drapatz, S., Eckart, A., Genzel, R., Hofmann, R., Loewe, M., & Sams, B. J. 1995, ESO Messenger, 79, 23
Bruzual, G., & Charlot, S. 1993, ApJ, 405, 538
Campbell, B., et al. 1992, AJ, 104, 1721
Cassinelli, J. P., Mathis, J. C., & Savage, B. D. 1981, Science, 212, 1497
Conti, P. S., Hanson, M. M., Morris, P. W., Willis, A. J., & Fossey, S. J. 1995, ApJ, 445, L35
Crowther, P. A., & Smith, L. J. 1996, A&A, 305, 541
de Marchi, G., Nota, A., Leitherer, C., Ragazzoni, R., & Barbieri, C. 1993, ApJ, 419, 658
Eckart, A., & Duhoux, P. R. M. 1990, in Astrophysics with Infrared Arrays, ed. R. Elston (San Francisco: ASP), 336
Eenens, P. R. J., Morris, P. W., van Kerkwijk, M., Tapia, M., & Williams, P. M. 1995, in preparation
Elson, R. A. W., Schade, D. J., Thomson, R. C., & Mackay, C. D. 1992, MNRAS, 258, 103
ESO. 1995, Applications for Observing Time at LaSilla—Period 56
Fitzpatrick, E. L. 1985, ApJ, 299, 219
Heap, S. R., Ebbets, D., Malumuth, E. M., Maran, S. P., de Kotter, A., & Hubeny, I. 1994, ApJ, 435, L39
Hill, J. K., Isensee, J. E., Cornett, R. H., Bohlin, R. C., O'Connell, R. W., Roberts, N. S., Smith, A. M., & Stecher, T. P. 1994, ApJ, 425, 122
Hofmann, R., Brandl, B., Eckart, A., Eisenhauer, F., & Tacconi-Garman, L. 1995, Proc. SPIE, 2475, 192
Hook, R., Lucy, L., Stockton, A., & Ridgway, S. 1994, ST-ECF Newsletter 21, 17
Hubin, N., Beuzit, J.-L., Gendron, E., & Demailly, L. 1993, in ICO16 Satellite Conference on Active and Adaptive Optics, (Garching: ESO Conf. and Workshop Proc. 48), 71
Hunter, D. A., Shaya, E. J., Hotlzman, J. A., Light, R. M., O'Neil, E. J., Jr., & Lynds, R. 1995, ApJ, 448, 179
Hyland, A. R., Straw, S., Jones, T. J., & Gatley, I. 1992, MNRAS, 257, 391
Johnson, H. L., & Morgan, W. W. 1953, ApJ, 117, 313
Kennicutt, R. C. 1984, ApJ, 287, 116
Kennicutt, R. C., & Chu, Y.-H. 1994, in Violent Star Formation, ed. G. Tenorio-Tagle (Cambridge: Cambridge Univ. Press), 1
King, I. R. 1962, AJ, 67, 471
Kontizas, M., Kontizas, E., & Michalitsianos, A. G. 1993, A&A, 269, 107
Kunze, D., Kudritzky, R. P., & Puls, J. 1992, in The Atmospheres of Early Type Stars, ed. U. Heber & C. S. Jeffery (Berlin: Springer), 45
Kurucz, R. L., 1992, in IAU Symp. 149, The Stellar Population of Galaxies, ed. B. Barbuy & A. Renzini (Dordrecht: Kluwer), 225
Lattanzi, M. G., et al. 1994, ApJ, 427, L21
Léna, P. J. 1994, Proc. SPIE 2201, 1099
Lightman, A. P., & Shapiro, S. L. 1978, Rev. Mod. Phys., 50(2), 437
Lucy, L. B. 1974, AJ, 79, 745
———. 1994, in the Restoration of HST Images and Spectra, ed. R. J. Hanisch & R. L. White (Baltimore: STScI), 79
Maeder, A., & Meynet, G. 1993, A&A, 287, 803
Malumuth, E. M., & Heap, S. R. 1994, AJ, 107, 1054
Massey, P., Garmany, C. D., Silkey, M., & DeGioia-Eastwood, K. 1989, AJ, 97, 107
Massey, P., Lang, C. C., DeGioia-Eastwood, K., & Garmany, C. D. 1995, ApJ, 438, 188
Melnick, J. 1985, A&A, 153, 235
———. 1992, Star Formation in Stellar Systems (Cambridge: Cambridge Univ. Press)
Meylan, G. 1993, in ASP Conf. Ser. 48, The Globular Cluster-Galaxy Connection, ed. G. H. Smith & J. P. Brodie (San Francisco: ASP), 588
Meynet, G., Maeder, A., Schaller, G., Schaerer, D., & Charbonnel, C. 1994, A&AS, 103, 97
Miller, G. E., & Scalo, J. M. 1979, ApJS, 41, 513
Moffat, A. F. J., Seggewiss, W., & Shara, M. M. 1985, ApJ, 295, 109
Parker, J. Wm. 1993, AJ, 106, 560
Parker, J. Wm., & Garmany, C. D. 1993, AJ, 106, 1471
Parker, J. Wm., Heap, S. R., & Malumuth, E. M. 1995, ApJ, 448, 705
Poglitsch, A., Krabbe, A., Madden, S. C., Nikola, T., Geis, N., Johansson, L. E. B., Stacey, G. J., & Sternberg, A. 1995, ApJ, 454, 293
Rieke, G. H., & Lebofsky, M. J. 1985, apJ, 288, 618
Rubio, M., Roth, M., & García, J. 1992, A&A, 261, L29
Salpeter, E. E. 1955, ApJ, 121, 161
Sams, B. J., III, 1995, ApJ, 445, 221
Schaerer, D., Meynet, G., Maeder, A., & Schaller, G. 1993, A&AS, 98, 523
Schild, H., & Testor, G. 1992, A&AS, 92, 729
Spitzer, L., Jr. 1987, Dynamical Evolution of Globular Clusters (Princeton: Princeton Univ. Press)
Stetson, P. B. 1987, PASP, 99, 191
Walborn, N. R. 1991, in IAU Symp. 148, The Magellanic Clouds, ed. R. F. Haynes & D. K. Milne (Dordrecht: Kluwer), 145
Walborn, N. R., Ebbets, D. C., Parker, J. Wm., Nichols-Bohlin, J., & White, R. L. 1992, ApJ, 393, L13
Weigelt, G., & Baier, G. 1985, A&A, 150, L18
Weigelt, G., et al. 1991, ApJ, 378, L21
West, R. 1995, private communication